

PERFORMANCE ASSESMENT OF INDIUM ANTIMONIDE
PHOTODETECTORS ON SILICON SUBSTRATES

A THESIS SUBMITTED TO
THE GRADUATE SCHOOL OF NATURAL AND APPLIED SCIENCES
OF
THE MIDDLE EAST TECHNICAL UNIVERSITY

BY

ÜMİD TÜMKAYA

IN PARTIAL FULFILLMENT OF THE REQUIREMENTS FOR THE DEGREE OF
MASTER OF SCIENCE
IN
THE DEPARTMENT OF PHYSICS

JUNE 2003

Approval of Graduate School of Natural and Applied Sciences.

Prof. Dr. Canan ÖZGEN
Director

I certify that this thesis satisfies all the requirements as a thesis for the degree of Master of Science.

Prof. Dr. Sinan BİLİKMEN
Head of Department

We certify that we have read this thesis and that in our opinion it is fully adequate, in scope and quality, as a thesis for the degree of Master of Science.

Assoc. Prof. Dr. Cengiz BEŞİKÇİ
Co-Supervisor

Prof. Dr. İbrahim GÜNAL
Supervisor

Examining Committee Members:

Prof. Dr. Çiğdem ERÇELEBİ

Prof. Dr. İbrahim GÜNAL

Assoc. Prof. Dr. Cengiz BEŞİKÇİ

Prof. Dr. Raşit TURAN

Prof. Dr. Bülent AKINOĞLU

ABSTRACT

PERFORMANCE ASSESMENT OF INDIUM ANTIMONIDE PHOTODETECTORS ON SILICON SUBSTRATES

TÜMKAYA, Ümid

M.Sc., Department of Physics

Supervisor: Prof. Dr. İbrahim GÜNAL

Co-Supervisor: Assoc. Prof. Dr. Cengiz BEŞİKÇİ

June 2003, 85 pages

In this study, detailed characteristics and performance assessment of 3–5 μm p-i-n InSb photodetectors on Si substrates are reported. The detector epilayers were grown on GaAs coated Si substrates by molecular beam epitaxy (MBE). Both homojunction and single heterojunction (AlInSb/InSb) detector structures were investigated. Arrays of $33 \times 33 \mu\text{m}^2$ detectors were fabricated and flip-chip bonded to a test substrate for detailed electrical and optical characterization. A peak detectivity as high as $1 \times 10^{10} \text{ cmHz}^{1/2}/\text{W}$ was achieved with InSb homojunction detectors on Si substrate in spite of the large lattice mismatch between InSb and Si (%19). In both homojunction and single heterojunction structures the differential resistance is significantly degraded by trap assisted tunneling (TAT) under

moderately large reverse bias and by ohmic leakage near zero-bias. While the heterojunction structures provide a higher 80 K zero bias differential resistance, the responsivity of this structure is significantly lower than that of homojunction InSb photodiodes. In both homojunction and heterojunction photodetectors, 80K $1/f$ noise is dominated by TAT processes, and the noise current at 1 Hz follows the empirical relation $i_n = \alpha_{TAT}(I_{TAT})^\beta$ with $\alpha_{TAT} \sim 1.1 \times 10^{-6}$ and $\beta \sim 0.53$.

Keywords: photodetector, AlInSb, InSb, focal plane array

ÖZ

SİLİSYUM TABAN ÜZERİNDE İNDİYUM ANTİMON FOTODEDEKTÖRLERİNİN PERFORMANS DEĞERLENDİRMESİ

TÜMKAYA, Ümid

Yüksek Lisans, Fizik Bölümü

Tez Yöneticisi: Prof. Dr. İbrahim GÜNAL

Ortak Tez Yöneticisi: Doç. Dr. Cengiz BEŞİKÇİ

Haziran 2003, 85 sayfa

Bu çalışmada Si taban üzerine büyütülmüş 3-5 μm p-i-n InSb fotodedektörlerin detaylı karakteristikleri ve performans değerlendirmesi rapor edilmiştir. Dedektör katmanları GaAs kaplı Si taban üzerine moleküler ışın epitaksisi ile (MBE) büyütülmüş hem homoeklem hem de tek heteroeklem (AlInSb/InSb) dedektör yapıları üzerinde çalışılmıştır. $33 \times 33 \mu\text{m}^2$ alanlı dedektör dizinleri üretilmiş ve detaylı elektriksel ve optik karakterizasyon testleri için test tabanları üzerine flip-chip bağlama yöntemiyle entegre edilmiştir. Si ve InSb arasındaki yüksek örgü uyumsuzluğuna rağmen (%19) Si üzerine InSb homoeklemlili dedektör için $1 \times 10^{10} \text{ cmHz}^{1/2}/\text{W}$ gibi yüksek bir tepe dedektivite değeri elde edilmiştir. Diferansiyel direnç hem homoeklem hem de tek

heteroeklem yapılarında orta mertebede ters gerilimlerde tuzak yardımcı tünelleme mekanizması tarafından, sıfır eğimleme yakınında ohmik kaçak mekanizmaları tarafından kayda değer bir şekilde düşürülmektedir. 80 K sıcaklıkta heteroeklem yapısı daha yüksek sıfır gerilim diferansiyel direnç vermesine rağmen bu yapının optik duyarlılığı homoeklem InSb fotodiyotlarından oldukça düşüktür. Hem homoeklem, hem de heteroeklem fotodedektörlerde, 80 K sıcaklıkta 1/f gürültüsü tuzak yardımcı tünelleme mekanizması tarafından belirlenmekte ve heteroeklem dedektör için 1 Hz'teki gürültü akımı $i_n = \alpha_{TAT}(I_{TAT})^\beta$ eşitliğine $\alpha_{TAT} \sim 1.1 \times 10^{-6}$ ve $\beta \sim 0.53$ katsayılarıyla uyum sağlamaktadır.

Anahtar Kelimeler: fotodedektör, AlInSb, InSb, odak düzlem matrisi

To my wife and my coming baby...

ACKNOWLEDGMENTS

I would like to thank my thesis advisors Prof. Dr. İbrahim Gnal and Assoc. Prof. Dr. Cengiz Beşikçi for their guidance and support. I would like to acknowledge Selçuk zer for his collaboration in the fabrication, testing and modeling of InSb photodetectors and Oray Orkun Celtek for his help in the optical characterization of photodetectors.

This research is a part of the KOBRA project, which is sponsored by Turkish Ministry of Defense, TBİTAK, and ASELSAN Inc. in the framework of the Development of Infrared Detector Focal Plane Arrays for Thermal Imaging.

TABLE OF CONTENTS

ABSTRACT	iii
ÖZ.....	v
ACKNOWLEDGMENTS	viii
TABLE OF CONTENTS.....	ix
LIST OF FIGURES	xi
LIST OF TABLES	xiv
LIST OF SYMBOLS	xv
CHAPTERS	
1. INTRODUCTION.....	1
1.1 Scope and Objectives of the Study	2
1.2 Organization of the Thesis.....	3
2. INFRARED DETECTORS AND THERMAL IMAGING.....	5
2.1 Infrared Radiation	5
2.2 Infrared Detectors	7
2.2.1 Thermal Detectors	9
2.2.2 Photon Detectors	11
2.2.2.1 Photovoltaic Detectors	13

2.2.2.2 Photoconductive Detectors	17
2.2.2.3 Quantum Well Infrared Photodetectors	18
2.3 Focal Plane Arrays.....	19
2.4 Infrared Detector Parameters.....	22
2.5 Materials for Infrared Detectors	30
2.6 Thermal Imaging.....	36
3. TEST DETECTOR FABRICATION AND CHARACTERIZATION.....	39
3.1 Semiconductor Structures Used for Detector Fabrication	39
3.2 Fabrication of Test Detectors.....	42
3.2.1 Test Read-Out Circuit Fabrication	50
3.3 Electrical Characterization.....	51
3.4 Dark Current	53
3.4.1 Diffusion Current	54
3.4.2 Generation-Recombination Current	55
3.4.3 Tunneling Current	56
3.4.4 Ohmic Leakage Current	58
3.4.5 Analysis of Dark Current	58
3.5 Detector Noise	67
3.6 Optical Characterization	72
4. 128x128 ARRAY FABRICATION AND TESTING	76
4.1 Fabrication of 128x128 Detector Arrays	76
4.2 Real Time Thermal Imaging.....	79
5. CONCLUSION.....	80
REFERENCES.....	82

LIST OF FIGURES

FIGURES

2.1 Electromagnetic spectrum.....	6
2.2 Schematic Representation of the operation of a p-n Junction Photodiode [2]...	14
2.3 One Dimensional Model of a p-n junction	14
2.4 <i>V-I</i> Curve of a Photodiode	15
2.5 Photoconductive IR detector structure and its energy band diagram.....	17
2.6 Comparison of conventional discrete detector configurations versus IRFPAs. (a) Single element detector with dedicated preamp performing a sequence of horizontal scans. (b) Multiple detectors, each with a dedicated preamp performing a parallel scan. (c) Linear array with CCD multiplexer and preamp performing parallel scan. (d) TDI array with multiplexer and preamp performing parallel scan (Horizontal delay devices not shown). (e) Staring array detector (Horizontal and vertical charge transfer devices not shown).....	20
2.7 Noise is “clutter” that degrades signal fidelity: (a) with little noise; (b) with more noise	23
2.8 Frequency Spectrum of noise.....	24
2.9 Detector output with varying signal-to-noise ratios.....	25
2.10 Signal vs Incidence plot showing linear and saturated regions.....	27
2.11 Frequency response.....	28
2.12 Crosstalk due to optical reflections and electrical coupling.....	30
3.1 <i>E-k</i> diagram of Insb.....	40
3.2 Energy band diagram of AlInSb/InSb/InSb heterojunction.....	41

3.3 Semiconductor wafer structures used in this study (a) AlInSb/InSb heterojunction on Si substrate (b) InSb homojunction on Si substrate.	41
3.4 Semiconductor substrate coated by photoresist	44
3.5a Photolithography	44
3.5b Developed Photoresist.....	45
3.6a Etched Substrate	46
3.6b Photoresist removed after etching.....	46
3.7a Passivation coated substrate	46
3.7b PR is developed and passivation openings are formed	46
3.7c Passivated substrate except for top of the diodes	46
3.8a Developed PR for metal deposition.....	47
3.8b Deposited Metal	47
3.8c The unnecessary metal layers are removed by lift-off	47
3.9 The setup for electroplating	48
3.10 The In plated sample	49
3.11 Indium bumps formed after reflow	49
3.12 Flip-chipped detector array and read-out integrated circuit	50
3.13 Fabricated test read-out substrate.....	50
3.14 The test detector and fan-out substrate pair on an alumina substrate	51
3.15 Test set up for current-voltage measurements of the detectors.....	51
3.16 I - V characteristic and R_D of AlInSb/InSb/InSb detector at 77K	52
3.17 I - V characteristic and R_D of InSb/InSb/InSb detector at 77K	53
3.18 R_D vs. V graph of InSb/InSb/InSb from 80K to 240K	62
3.19 R_D vs. V characteristics of AlInSb/InSb/InSb from 80K to 240K.....	62
3.20 The fitting result of R_D for InSb/InSb/InSb detectors at 80K.	63
3.21 The fitting result of R_D for AlInSb/InSb/InSb detectors at 80K.	64
3.22 Fitting results of InSb/InSb detector at different temperatures	65
3.23 Fitting results of AlInSb/InSb/InSb at different temperatures.....	65
3.24 R_D vs. T for InSb/InSb/InSb at different bias voltages.....	66
3.25 R_D vs. T for AlInSb/InSb/InSb at different bias voltages.....	67
3.26 Equivalent circuit for noise measurement	68
3.27 Reverse bias dependence of $1/f$ noise of AlInSb/InSb/InSb detector	69

3.28 The components contributing to total $1/f$ noise for AlInSb/InSb/InSb detector at 90K and 120K.....	71
3.29 Responsivity and noise measurement setup.....	73
3.30 Detector spectral response measurement setup.....	74
3.31 The spectral response of AlInSb/InSb/InSb detector at 80 K.	74
3.32 The spectral response of InSb/InSb/InSb detector at 80 K.	75
4.1 The picture of etched mesa structures.....	77
4.2 The fabricated array with indium bumps.....	78
4.3 Flip-chip integrated detector array and ROIC were placed in LCC package	78
4.4 Infrared image of candlelight from 128x128 AlInSb/InSb/InSb heterojunction detector	79

LIST OF TABLES

TABLES

2.1: The performance of the $\text{In}_{1-x}\text{Tl}_x\text{Sb}$ photodetectors at 77K.....	36
3.1 Mask types according to process to be done and photoresist used	43
3.2 The calculated values of fitting parameters for different temperatures for AlInSb/InSb/InSb heterostructure detector	60

LIST OF SYMBOLS

W_λ	Spectral radiant emittance at wavelength λ ($\text{J sec}^{-1} \text{ m}^{-3}$)
T	Temperature (K)
h	Planck's constant (6.6256×10^{-34} J.s)
c	The speed of light in vacuum (2.998×10^{10} cm/s)
k	Boltzmann constant (1.381×10^{-23} J/K)
q	Electric charge (1.6×10^{-19} C)
ν	Frequency of electromagnetic wave (Hz)
λ	Wavelength (μm)
λ_c	Cut off wavelength (μm)
E_g	Band gap energy (eV)
A	Area (cm^2)
A_d	Detector area (cm^2)
η	Quantum efficiency
Φ	The incident photon flux density ($\text{cm}^{-2}\text{s}^{-1}$)
I	Current (A)
I_d	Dark current (A)
V	Voltage (V)
V_{bi}	Built-in voltage (V)
I_{ph}	Photocurrent (A)
R	Resistance (Ω)
R_s	Series Resistance (Ω)
R_{sh}	Shunt Resistance (Ω)
R_D	Differential Resistance (Ω)

R_0	Zero-bias differential Resistance (Ω)
J_{drift}	Drift current density (A/cm^2)
J_{diff}	Diffusion current density (A/cm^2)
E_a	Activation energy (eV)
\mathcal{R}	Responsivity (V/W for voltage responsivity, I/W for current responsivity)
f	Frequency (Hz)
S/N	Signal-to-noise ratio
NEP	Noise Equivalent Power (W)
NEP'	Noise Equivalent power per unit bandwidth ($W/Hz^{1/2}$)
D^*	Detectivity ($cm \cdot Hz^{1/2}/W$ or Jones)
$NETD$	Noise equivalent temperature difference (mK)
I_{DIFF}	Diffusion current (A)
I_{GR}	Generation-recombination current (A)
I_{TAT}	Trap assisted tunneling current (A)
I_{BTB}	Band-to-band tunneling current (A)
I_S	Shunt current (A)
J_{DIFF}	Diffusion current density (A/cm^2)
J_{GR}	Generation-recombination current density (A/cm^2)
J_{TAT}	Trap assisted tunneling current density (A/cm^2)
J_{BTB}	Band-to-band tunneling current density (A/cm^2)
J_S	Shunt current density (A/cm^2)
D_n	Diffusion constant for electrons (cm^2/sec)
D_p	Diffusion constant for holes (cm^2/sec)
L_n	Diffusion length for electrons (cm)
L_p	Diffusion length for holes (cm)
μ_n	Electron mobility ($cm^2/V\text{-sec}$)
μ_p	Hole mobility ($cm^2/V\text{-sec}$)
τ_n	Electron lifetime (sec)
τ_p	Hole lifetime (sec)
n	Free carrier electron concentration (cm^{-3})
p	Free carrier hole concentration (cm^{-3})

W, x_d	Width of depletion region (cm)
W_0	Zero bias depletion layer width (cm)
s_0	Surface recombination velocity ()
E_F	Fermi level for a semiconductor (eV)
E_i	Intrinsic energy level for a semiconductor (eV)
E_t	Trap energy level for a semiconductor (eV)
E_c	Conduction band level for a semiconductor (eV)
E_v	Valance band level for a semiconductor (eV)
N_d	Donor concentration (cm^{-3})
N_a	Acceptor concentration (cm^{-3})
E	Electric field (V/cm)
m_e	Electron mass (kg)
m_h	Hole mass (kg)
c_n	Capture coefficient of electrons (cm^3/s)
c_p	Capture coefficient of holes (cm^3/s)
m_e^*	Effective mass of electrons (kg)
m_h^*	Effective mass holes (kg)
N_c	Effective density of states in the conduction band (cm^{-3})
N_v	Effective density of states in the valance band (cm^{-3})
R_{DIFF}	Differential resistance for diffusion mechanism (Ω)
R_{GR}	Differential resistance for generation-recombination mechanism (Ω)
R_{TAT}	Differential resistance for trap assisted tunneling mechanism (Ω)
R_{BTB}	Differential resistance for band-to-band tunneling mechanism (Ω)
R_{SHUNT}	Differential resistance for shunt mechanism (Ω)
ϵ	Dielectric constant (F/cm)
i_n	Noise current spectral density ($\text{A}/\text{Hz}^{1/2}$)
α	Hooge's parameter
β	Hooge's parameter
v_s	saturation velocity (cm/s)

CHAPTER I

INTRODUCTION

Recent success in applying infrared (IR) technology to remote sensing problems become possible due to successful development of high performance IR detectors over the last few decades. Many materials have been investigated in the infrared field. Interest has centered mainly on the wavelengths of the two atmospheric windows 3-5 μm and 8-12 μm , though in recent years there has been increasing interest in longer wavelengths stimulated by space applications.

Photodiodes with their low power dissipation, easy multiplexing on focal plane silicon chip and less stringent noise requirements for the read-out devices and circuits, can be assembled in two-dimensional (2-D) arrays containing a very large ($\approx 10^6$) number of elements, limited only by existing technologies. Systems based on such focal plane arrays (FPAs) can be smaller, lighter, need lower power consumption, and can result in much higher performance than systems based on first generation detectors. Photodiodes can also have low noise, faster response time, and the potential for a uniform spatial response across each element. However, the more complex processes needed for photovoltaic detectors have influence on slower development and industrialization of the second-generation systems, particularly for large arrays.

Indium antimonide (InSb) is an important III-V semiconductor for both optical and electronic applications. InSb offers important advantages over HgCdTe, other widely used infrared material, such as relatively easy large area homogenous growth and stronger covalent bonding. This material is far more mature than HgCdTe and good quality more than 7 cm diameter bulk substrates are commercially available. InSb photodiodes have been available since the late fifties and they are generally fabricated by impurity diffusion, ion implantation and epitaxy. It has the highest intrinsic electron mobility and the smallest band gap (0.227 eV at 77 K) of all binary III-V compounds.

InSb on GaAs or Si substrates has very important advantages due to the availability of large area GaAs or Si wafers. These substrates are stronger, more suitable for mass production and lower in cost when compared to other substrates. Si substrate has also the same thermal expansion coefficient with read-out circuit and eliminates the need for substrate removal process. However, the large lattice mismatch between InSb and these substrates is the limiting factor for the growth of high quality InSb detector materials on GaAs and Si substrates.

1.1 Scope and Objectives of the Study

The aim of this study is to assess the performance of AlInSb/InSb heterojunction and InSb homojunction p-i-n detectors and focal plane arrays grown on GaAs coated Si substrates by molecular beam epitaxy. The scope of our study can be summarized as follows:

- A literature survey on different infrared materials. For this purpose, previous studies on widely used infrared detector materials, such as HgCdTe, PtSi, InAsSb, InSbBi, InAsBi, InAsSbBi, GaInSbBi, InTlSb, InTlP, and InTlAs, were studied and summarized in the scope of the thesis.
- Design of the required masks and fabrication of p-i-n photodetector

arrays by using the detector layer structures grown on GaAs coated Si substrates at Northwestern University. For this purpose, CADENCE VLSI DESIGN tool was used to design the fabrication masks. The mask design and the fabrication of the photodetectors were completed METU Electrical and Electronics Department under support of ASELSAN Inc. 128x128 detector arrays were fabricated for characterization and thermal imaging.

- Detailed electrical and optical characterization of the fabricated detectors and interpretation of the results through modeling in order to assess the feasibility of large area InSb focal plane arrays on Si substrates.

1.2 Organization of the Thesis

The organization of the thesis is as follows:

Chapter II introduces fundamentals of infrared radiation, infrared detectors, and thermal imagers. It describes different types of infrared detectors and detector arrays. This chapter also includes a literature survey on the studies made by other research groups on various infrared detector materials.

Chapter III describes the design of fabrication masks and the process steps for the fabrication of the detector arrays. The fabrication procedure is presented in detail as well as the mask design.

Chapter IV presents the results and test setups for electrical and optical characterization, followed by a comparison of our results with those of other research groups. The results of the study on dark current analysis at different temperatures are presented. The interpretation of the results and some suggestions for the improvement of detector performance are also given in this chapter.

Chapter V presents the results of measurements on the carrier life times in AlInSb/InSb/InSb heterostructures and InSb/InSb/InSb homostructures grown on GaAs and Si substrates.

Finally, Chapter VI summarizes the results and conclusions of this study.

CHAPTER II

INFRARED DETECTORS AND THERMAL IMAGING

2.1 Infrared Radiation

Infrared radiation is a form of radiated electromagnetic energy, obeying the same laws as those for visible light, radio waves, and X-rays [1]. Figure 2.1 shows the electromagnetic spectrum from UV to far-infrared range. Infrared radiation extends from $0.7 \mu\text{m}$ to $1000 \mu\text{m}$ in the electromagnetic spectrum.

All objects above absolute zero (0K or -273°C) emit infrared radiation. Peak emission from the objects at room temperature occurs at wavelength of $10 \mu\text{m}$. On the other hand, hot objects radiate at shorter wavelengths.

The earth's atmosphere limits which wavelengths can be used in infrared imaging because infrared radiation is strongly absorbed by water vapor and carbon dioxide. There are, however, several wavelength bands or windows with good transmission. These bands are;

- Long Wavelength Infrared (LWIR): in the $8\text{-}14 \mu\text{m}$ wavelength range, which provides excellent visibility of most terrestrial objects.

- Mid Wave Infrared (MWIR): in the 3-5 μm wavelength range for viewing either hotter objects or room temperature objects.
- Short Wave Infrared (SWIR): in the 1.5-1.8 and 2.0-2.4 μm wavelength ranges.
- Near Infrared (NIR): in the 0.7-1.1 μm wavelength range.

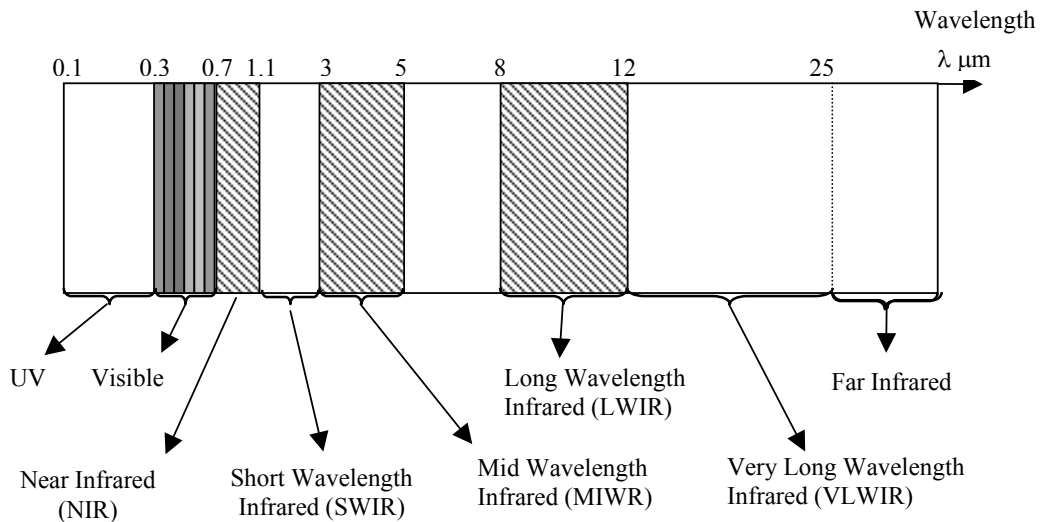


Figure 2.1 Electromagnetic spectrum

The primary bands for thermal imaging are the LWIR and MWIR bands. The SWIR and NIR bands are useful only for very hot objects or for specialized spectroscopic applications. However, recently, there has been a great deal of interest in using the SWIR band for low-light-level detection (i.e. not for passive thermal imaging but in a reflected light mode).

The decision as to which band to use for a particular application depends upon numerous factors. For example, reflections can complicate temperature measurements. Since ground-level solar radiation contains significant energy in the 3-5 μm band, this is particularly true of reflected sun light. Thus, for many outdoor measurements the 8-12 μm band is preferred. However, for hotter objects the 3-5

μm band may be more appropriate, essentially since the detector itself can be operated at higher temperature.

For space applications, Very Long Wave Infrared (VLWIR) region is usually preferred and these applications often require specialty sensors operating at wavelengths up to 100 μm .

2.2 Infrared Detectors

Infrared detectors and detector arrays are used in many civilian and defense oriented applications today. These applications are usually based on passive detection of thermally emitted electromagnetic radiation as described by the well-known Planck's law, which employs the concepts of statistical thermodynamics.

$$\frac{dR(\lambda, T)}{d\lambda} = \frac{2\pi hc^2 \lambda^{-5}}{\exp\left(\frac{hc}{\lambda kT}\right) - 1} \quad 2.1$$

where $\frac{dR(\lambda, T)}{d\lambda}$ is the spectral exitance (power emitted per unit area and unit wavelength)

$c = 2.998 \times 10^8 \text{ ms}^{-1}$ speed of light in vacuum

$h = 6.6256 \times 10^{-34} \text{ Js}$ Planck's constant

$\lambda =$ wavelength

$k = 1.38054 \times 10^{-23} \text{ JK}^{-1}$ Boltzmann constant

$T =$ Absolute temperature in K.

In this way, it is possible to image objects in darkness, or carry out contactless temperature measurement. Active systems, on the other hand, are based on the illumination of the object by an infrared source, such as a thermal emitter or an infrared laser. Laser radar is an example of active systems.

Planck's radiation law states that every object at a temperature above absolute zero emits electromagnetic radiation, and the higher the temperature the higher is the emitted intensity. In addition, the wavelength of maximum intensity decreases when the temperature increases (Wien's displacement law). Planck's law is strictly valid only for ideal blackbodies, which by definition have 100 % absorption and maximum emitting intensity (i. e. exitance). Real objects can be handled by introducing emissivity, a factor less than unity, equal to the ratio of the emitting intensity of the object and that of a corresponding blackbody having the same temperature as the object. The emissivity is generally wavelength dependent. Objects with a less than unity and almost constant emissivity are named graybodies.

Usually infrared imaging is performed in either of two different atmospheric transmission windows: the 3-5 μm range MWIR - Medium Wavelength Infrared, or the 8-12 μm range LWIR - Long Wavelength Infrared. In these windows, atmospheric transmission is maximum or equivalently the absorption is minimum. However, some applications such as gas analysis are performed at wavelengths where the absorption is maximum, i. e. 4.2 μm for carbon dioxide and around 6 μm for water vapor.

It is notable, that in a global perspective, for many years all the major breakthroughs in infrared technology, and the major purchases of infrared equipment, have been funded by military sponsors. Consequently, the technology has been developed with the military user in mind, and the emphasis been on high performance IR systems, predominantly cooled photon detectors. However, a main future trend will most certainly be to re-examine one of the strengths of infrared technology i. e. its suitability to applications outside the military sector, and meet the needs of the civil customer. The civil sector can accept a lower performance, but the price per unit must be kept low, and the equipment should be user friendly. The medium performance, uncooled thermal detector technology is certainly suitable for this. To reach the goals of a civil product can be at least equally technologically challenging as for R&D on high performance detector systems. A potentially important civilian market for uncooled infrared detector arrays is the car

industry (driver's aids) and surveillance systems for inspection purposes (e.g. radio stations, fire control, frontier control). Other areas are medical diagnostics and robotic manufacturing. When a higher performance is needed, the quantum well infrared photodetector (QWIP) technology is suitable. In spite of the fact that it is a cooled detector technology, detector arrays can be fabricated at a comparatively low cost.

2.2.1 Thermal Detectors

Thermal detectors absorb infrared radiation and undergo a slight temperature rise, which is then measured. The absorption of infrared radiation in these detectors raises the temperature of the device and changes some temperature-dependent parameter such as electrical conductivity. Thermal detectors may be thermopile (Seebeck effect), bolometer, Golay cell detectors, or pyroelectric detectors.

In fact, when Herschel discovered the infrared spectrum in the year 1800 he utilized a simple type of thermal detector, a liquid in a glass thermometer, which is considered the first thermal detector. The infrared radiation was absorbed by blackening the bulb of the thermometer.

The most significant advantage of thermal detectors is that they can operate at room temperature and can easily be fabricated to respond to all wavelengths. However, the sensitivity is lower and the response time is longer than that for photon detectors. This makes thermal detectors suitable for focal plane array operation, where the latter two properties are less critical although the latest generation of uncooled focal plane arrays has made significant advances in both of these areas.

A thermal detector is conveniently divided into three functional parts; an absorber for infrared radiation, a membrane or other structure for achieving thermal insulation and, a temperature detector.

In order to obtain high sensitivity it is of utmost importance that the detector element is thermally insulated from the detector substrate. Therefore, when fabricating thermal detector arrays it is common to make thin membranes using micro-mechanical processing techniques. The material may be silicon nitride or silicon dioxide, which both are compatible with silicon processing techniques.

The temperature detector is usually integrated into the membrane, and utilized to detect the usually minute temperature change resulting from exposure to infrared radiation from a room-temperature scene and subsequent absorption. Thermal detectors are conveniently classified according to their means of detecting this temperature change:

A resistive bolometer contains a resistive material, whose resistivity changes with temperature. To achieve high sensitivity the temperature coefficient of the resistivity should be as large as possible and the noise resulting from contacts and the material itself should be low. Resistive materials could be metals such as platinum, or semiconductors (thermistors). Metals usually have low noise but have low temperature coefficients (about 0.2 %/K), semiconductors have high temperature coefficients (1-4 %/K) but are prone to be noisier. Semiconductors used for infrared detectors are e.g. amorphous, polycrystalline silicon, or vanadium oxide.

A thermoelectric device (thermocouple or thermopile) is based on the presence of one or several junctions between two materials. The junctions properly arranged and connected develop a thermo-emf that changes with temperature, the so-called Seebeck effect. In order for the sensitivity to be high the Seebeck coefficient should be as high as possible. Certain alloys containing antimony and

bismuth have very high Seebeck coefficients of $150 \mu\text{V/K}$. The CMOS compatible combination aluminum/polycrystalline silicon gives about $65 \mu\text{V/K}$.

A pyroelectric detector is based on the fact that certain dielectric materials of low crystal symmetry exhibit spontaneous dielectric polarization. When the electric dipole moment depends on temperature the material becomes pyroelectric. Usually a capacitor is fabricated from the material and the variation of the capacitor charge is sensed. Common pyroelectric materials used for infrared detectors are TGS (tri-glycine sulphate), LiTaO_3 (lithium tantalate), PZT (lead zinc titanate) and certain polymers. A dielectric bolometer makes use of pyroelectric materials operated in a way to detect the change of the dielectric constant with temperature. A suitable material for this application is SBT (strontium barium titanate).

The Golay detector is based on the volume or pressure change of an encapsulated gas with temperature. The volume change is measured e.g. by the deflection of light rays resulting from the motion of properly positioned mirrors fastened to the walls of the gas container.

2.2.2 Photon Detectors

The photon detectors (or quantum detectors) are generally semiconductor devices in which the absorption of an infrared photon excites electrons from a bound state to a mobile state, thus producing a change in electrical conductivity or voltage. The spectrum of wavelengths absorbed depends upon the semiconductor's energy band gap – only those of wavelength shorter than the band gap (the “cut-off wavelength”) will be absorbed. They normally require cooling down to cryogenic temperatures in order to get rid of excessive dark current, but in return their general performance is higher, with larger detectivities and smaller response times.

Photon detectors can be subdivided into photoconductive and photovoltaic devices. The function of photoconductive detectors is based on the photogeneration

of charge carriers (electrons, holes or electron-hole pairs). These charge carriers increase the conductivity of the device material. Materials possible to utilize for photoconductive detectors are:

- Indium antimonide (InSb)
- AlGaAs/GaAs (for QWIPs)
- Mercury cadmium telluride (MCT)
- Lead sulfide (PbS)
- Lead selenide (PbSe)

Photovoltaic devices require an internal potential barrier with a built-in electric field in order to separate photo-generated electron-hole pairs. Such potential barriers can be created by the use of p-n junctions or Schottky barriers. Whereas the current-voltage characteristics of photoconductive devices are symmetric with respect to the polarity of the applied voltage, photovoltaic devices exhibit rectifying behavior. Examples of photovoltaic infrared detector types are:

- Indium antimonide (InSb)
- Mercury cadmium telluride (MCT)
- Platinum silicide (PtSi) - silicon Schottky barrier

Photon detectors may also be classified on the basis of whether the photo-transitions take place across the fundamental band gap of the infrared sensitive material, or from impurity states to either of the valence or the conduction band. In the first case, they are denoted intrinsic, in the latter case extrinsic. The quantum well type of detector discussed below is however not easily classified according to this criterion.

As mentioned above the cooling requirements of a detector are governed by the fact that dark current decreases with lower operating temperature. In addition, dark current increases with the larger cut-off wavelength of the detector (i.e. the largest wavelength at which the detector has a response). In general, for constant

cut-off wavelength and temperature, dark current is lower for intrinsic detectors than for extrinsic ones. Therefore, the cooling requirements are less pronounced for the former type.

In most cases photon detectors need to be cooled to cryogenic temperatures, i. e. down to 77 K (liquid nitrogen) or 4 K (liquid helium). In some favorable cases thermoelectric cooling down to 200 K is sufficient (e.g. 3 - 5 μm wavelength mercury cadmium telluride). The main workhorse in the field of photon detectors is mercury cadmium telluride or "MCT" (HgCdTe), and to some less extent indium antimonide (InSb). Vigorous work has been done on MCT both in US and Europe since its discovery in 1959 and work is still being done. MCT is used both for the 3 - 5 μm (MWIR) and 8 - 12 μm (LWIR) atmospheric transmission windows, whereas indium antimonide is solely for the 3 - 5 μm range. Platinum silicide (PtSi) Schottky barrier detectors also work in the MWIR domain. Large (512x512 pixels) PtSi focal plane arrays (FPA) have been fabricated, are compatible with silicon CCD/CMOS technology, and show high performance, due to the extremely good pixel to pixel uniformity, in spite of the very low quantum efficiency. For FPAs in the 3 - 5 μm window, MCT, InSb and PtSi materials pose no major technological problems and are considered to be a finished product. In contrast, to date, no photon detector FPAs operating in the 8 - 12 μm window exhibits superior performance when operated at 77-80 K.

2.2.2.1 Photovoltaic Detectors

In photovoltaic diodes, a built-in electric field is created by a diode structure in the semiconductor junction. This can be done by doping the semiconductor in layers (junction diode) or it can be done by forming a thin semi-transparent conductive layer on the front surface (Schottky-barrier diode). The absorption of a photon near this diode then gives rise to a voltage. Photovoltaic devices, which do not require a large external current, are easy to couple to read-out integrated

circuits, have higher frequency capability, and lower noise level. Photovoltaic effect can be observed in several structures. Examples of these structures are;

- p-n junctions
- Heterojunctions
- Schottky barriers
- Metal-insulator-semiconductor (MIS) photo-capacitors.

The most common one is the abrupt p-n junction, which is often referred to simply as a photodiode.

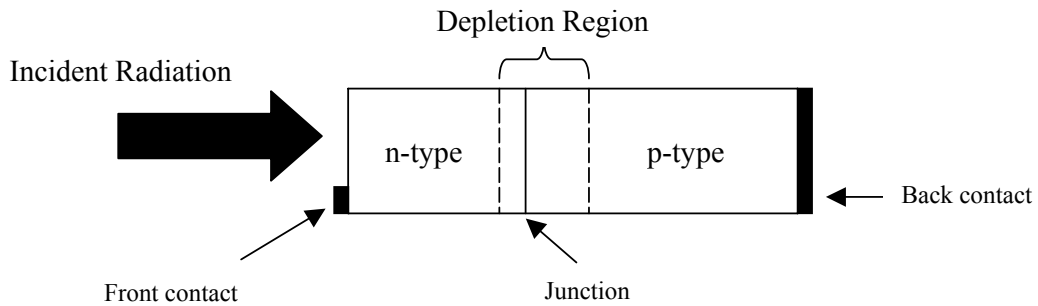


Figure 2.2 Schematic Representation of the operation of a p-n Junction Photodiode [2]

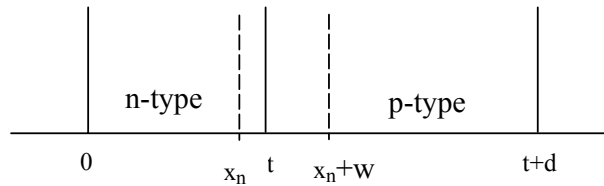


Figure 2.3 One Dimensional Model of a p-n junction [2]

Photons with energy greater than the energy gap, incident on the front surface of the device as shown in Figure 2.2, create electron-hole pairs in the material on both sides of the junction. By diffusion, the electrons and holes generated within a diffusion length from the junction reach the space charge region. The electron-hole pairs are separated by the strong electric field; minority carriers

are readily accelerated to become majority carriers on the other side. This way a photocurrent is generated which shifts the current-voltage characteristics in the direction of negative or reverse current, as shown in Figure 2.4. The magnitude of this photocurrent is

$$I_{ph} = \eta q A \Phi \quad 2.2$$

where A is the area of the photodiode, Φ is the incident photon flux density and η is the quantum efficiency.

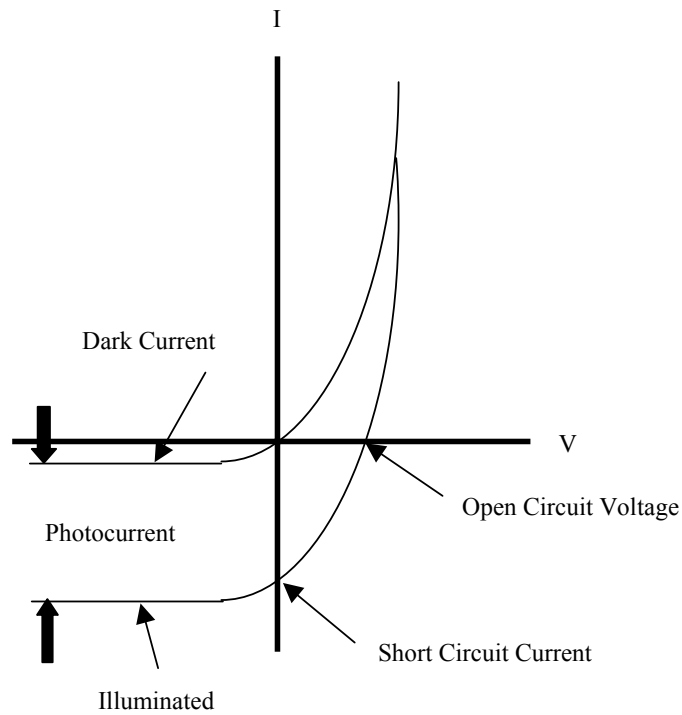


Figure 2.4 V-I Curve of a Photodiode [2]

If the p-n diode is open circuited the accumulation of electrons and holes on the two sides of the junction produces an open circuit voltage (Figure 2.4). If a load is connected to the diode, a current will flow through the circuit. The maximum current is realized when an electrical short is placed across the diode terminals, and this is called the short-circuit current.

The open circuit voltage can be obtained by multiplying the short-circuit current by the incremental diode resistance $R = \left(\frac{\partial I}{\partial V} \right)^{-1}$ at $V = V_b$.

$$V_{ph} = \eta q A \Phi R \quad 2.3$$

where V_b is the bias voltage. In many applications, the photodiode is operated near zero bias voltage with the dynamic resistance

$$R_o = \left(\frac{\partial I}{\partial V} \right)^{-1}_{|V_b=0} \quad 2.4$$

A frequently encountered figure of merit for a photodiode is the $R_o A$ product.

$$R_o A = \left(\frac{\partial J}{\partial V} \right)^{-1}_{|V_b=0} \quad 2.5$$

where $J = \frac{I}{A}$ is the current density. It is referred to often as the “ R -naught A -product”— $R_o A$ where R_o is calculated by drawing a line tangent to the curve at $V=0$ and determining the ratio $\frac{\Delta V}{\Delta I}$. This is a measure of the “health” of the diode.

Diodes with low resistance are “leaky” and tend to have high noise, or breakdown with time.

In the detection of radiation, the photodiode can be operated at any point of the V-I characteristics. Reverse bias operation is usually used for very high frequency applications to reduce the RC time constant of the device.

2.2.2.2 Photoconductive Detectors

The absorption of the photons increases the conductivity of the semiconductor and an electric circuit is used to measure the change in the resistance. These devices are easy to couple to low-noise preamplifiers but have the disadvantage of requiring an external current. This is the simplest detector structure using direct photon capture (as opposed to thermal detection). It can use either intrinsic or extrinsic semiconductors as shown in Figure 2.5.

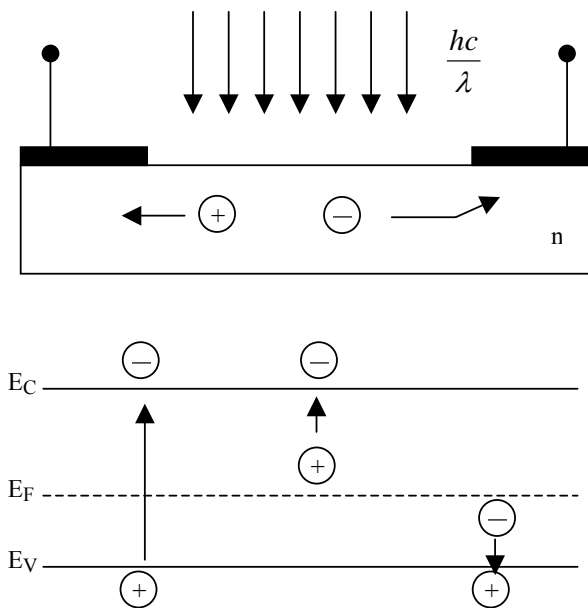


Figure 2.5 Photoconductive IR detector structure and its energy band diagram

The incoming photon energy, which must be greater than the energy gap of the semiconductor to be absorbed, excites an electron from the valence band into the conduction band leaving a hole in the valence band. Typically, electrons have much higher mobility values than holes in IR detector materials and hence, determine the photoresponse. In the case of extrinsic semiconductor, a photon is absorbed by an impurity with impurity ionization energy $E_a \approx h\nu$ and a free electron is created in a p-type semiconductor. Through this absorption process, a number of

free charge carriers are created resulting in a change in the conductivity of the semiconductor. When a constant bias is applied to the detector, the modulation in the current through the detector is proportional to the change in the photon flux incident on the detector.

Photoconductive detectors can exhibit gain, which is the ratio of the mean carrier lifetime to the transit time of the higher mobility free carrier across the detector between the two ohmic contacts. The gain may have a value from zero to greater than unity. In the latter case, the lifetime is greater than the transit time. Physically, this can be thought of as the free carriers transversing the detector (and the external circuit) several times before recombining.

2.2.2.3 Quantum Well Infrared Photodetectors

In the course of only the last 15 years, detectors based on low-dimensional structures have evolved as viable candidates for FPAs especially in the LWIR region. These so called band-gap engineered detectors operate on account of electronic transitions between electronic states arising as a result of size quantization, i.e. electron energy quantization due to the small layer dimensions in the growth direction. There are three main candidates of interest for IR detector arrays:

- the AlGaAs/GaAs quantum wells,
- the strained SiGe/Si superlattices (SL), and
- the strained InAs/GaInSb SLs.

The most mature is the AlGaAs/GaAs quantum well (QW) structure, which is a spin-off from GaAs technology. This detector type is generally named Quantum Well Infrared Photoconductor or QWIP. Here special grating structures are necessary in order to achieve a high quantum efficiency of the detector. QWIP

FPA's need operating temperatures around 70-75 K in order to work properly, temperatures, which are easily achievable by miniature Stirling coolers.

The main advantages of SiGe/Si QWs are the compatibility with silicon technology and that grating structures are not necessary. The cooling requirements seem, however, to be more extensive than for AlGaAs/GaAs quantum wells.

InAs/GaInSb so called type II SLs in theory offer the possibility of high sensitivity and operating temperatures of an intrinsic detector. In addition, the materials processing and uniformity are expected to be superior to for II-VI materials such as MCT. However, presently the maturity of the detector technology is far from being comparable to MCT detectors.

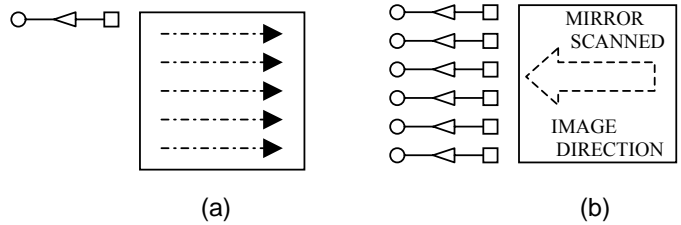
2.3 Focal Plane Arrays

Infrared focal plane arrays (IRFPAs) are critical components needed for advanced infrared imaging systems. Major advances in infrared detectors and microelectronics have led to the development of large area arrays of detectors fabricated using integrated circuit techniques. Traditionally, IRFPAs were either hybrid or monolithic architectures, but innovations in epitaxial growth of thin films now allow a number of useful variations.

There are a number of IRFPA detector configurations possible. These are compared with the conventional discrete infrared detector configurations in Figure 2.6. Two major advantages of IRFPAs are obvious. First, they provide an economical method for high-density packaging of detectors. Second, they allow signal processing to take place on the focal plane. Both of these advantages permit design tradeoffs of system parameters such as smaller optical apertures, reduced spectral bandwidth, and faster frame rates. Furthermore, other advantages are obtained in terms of eliminating much of the conventional processing circuitry (primarily involving preamplifiers and multiplexers attached to discrete detectors)

and reducing the number of signal leads through the dewar. When the multiplexing function is performed within the dewar, the overall system design becomes much simpler than the one involving discrete detectors and associated components.

CONVENTIONAL DISCRETE DETECTOR AND PREAMPLIFIER CONFIGURATIONS



IRFPA DETECTOR, MULTIPLEXER AND PREAMPLIFIER CONFIGURATIONS

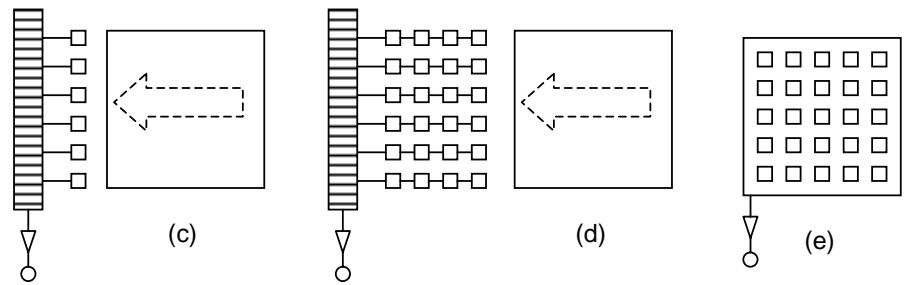


Figure 2.6 Comparison of conventional discrete detector configurations versus IRFPAs. (a) Single element detector with dedicated preamp performing a sequence of horizontal scans. (b) Multiple detectors, each with a dedicated preamp performing a parallel scan. (c) Linear array with CCD multiplexer and preamp performing parallel scan. (d) TDI array with multiplexer and preamp performing parallel scan (Horizontal delay devices not shown). (e) Staring array detector (Horizontal and vertical charge transfer devices not shown).

Several types of PtSi, InSb, HgCdTe, and QWIP arrays are available in the infrared market. 30x1, 60x1, and 120x1 HgCdTe scanning line arrays and 240x4, 288x4, 480x6, and 576x7 [3] HgCdTe scanning Time Delay Integration (TDI) arrays are manufactured for LWIR applications. There is a trend toward having higher number of detectors per chip in the infrared systems today. Large area PtSi IRFPAs have been fabricated as part of standard silicon processes and completely operational IRFPAs have been produced with 512x512 [4], 640x486 and

1024x1024 [5] for MWIR applications and even larger arrays of 2048x2048 are expected in the near future. InSb is currently being fabricated at the size of 256x256 [4], up to 1024x1024 [5] for the applications for the spectral range of 0.6-5 μm . MWIR HgCdTe staring arrays are available in the format of 128x128, 256x256, 320x256, 640x480, 640x512 [3][5][6]. Even 1024x1024 and 2048x2048 [5] HgCdTe staring arrays are fabricated for 1-2.5 μm applications. However, very large arrays (like 1028x1028) of HgCdTe for LWIR applications are not fabricated today due to material stability problems of this semiconductor in the corresponding spectral range. But, 128x128, 256x256, 320x256, 386x288 [3][5][6][7] format LWIR HgCdTe staring arrays can be supplied from the market. The first experimental studies on making use of quantum wells for infrared detection was made at the beginnings of 1980's [8]. Although QWIP technology is a young and developing technology compared with InSb and HgCdTe, large QWIP arrays are available. LWIR and MWIR 128x128, 256x256, 640x486, and 640x512 arrays are manufactured [5][6]. In addition, 128x128 and 320x240 InGaAs QWIPs are manufactured for 0,9-1,7 μm SWIR applications [5].

Several applications such as target recognition and discrimination require mid- and long-wavelength dual band large-area, uniform, reproducible, low cost and low noise infrared FPAs [8]. Reine *et al.* [9] reported results for 64x64 simultaneous MW/LW dual-band HgCdTe FPAs with cutoff wavelengths at 78K in the 4.27-4.35 μm and 10.1-10.5 μm ranges, respectively. Gunapala *et al.* [10] designed an optimized long-wavelength two-color QWIP structure, which was grown on 3-inch semi-insulating GaAs substrate by MBE. The wafer was processed into several 640x486 format monolithically integrated 8-9 and 14-15 μm two-color QWIP FPAs.

2.4 Infrared Detector Parameters

Responsivity

Responsivity is an important parameter of the detector. It allows users to determine ahead of time how sensitive a measuring circuit they will require to see the expected output, or how much amplifier gain they need to get the signal levels up to a satisfactory level. Alternatively, it tells them how to determine from the output signal what the detected incidence level was. Low responsivity is not itself an insurmountable problem; it is always possible to increase signal levels by adding amplifiers to the signal processing. The basic function of a detector is to convert the radiant input to an output signal of some convenient type. The output is electrical—either a current or a voltage. The responsivity \mathfrak{R} is the ratio between the output signal and the radiant input.

$$\mathfrak{R} = \frac{\text{signal output}}{IR \text{ input}} \quad 2.6$$

The IR input is the product of the incidence (the flux density of the incident waves to the detector, E) and the detector area, A_d .

$$IR \text{ input} = EA_d \quad (\text{the incident power}) \quad 2.7$$

$$\Rightarrow \mathfrak{R} = \frac{S}{E.A_d} \quad \frac{\text{Volt}}{\text{Watt}} \quad 2.8$$

Noise

It refers to an electrical output other than the desired signal. It is unavoidable, but we strive to keep it as low as possible. Once noise enters the output, it can obscure or completely hide the small signals. Some noise signals are fundamental, and for several reasons, cannot be avoided. A few of the reasons are:

- Photons do not arrive at an absolutely constant rate (the arrival rate fluctuates slightly)
- Atoms in the detector vibrate slightly, even at low temperatures.
- Electrons move randomly in the detector, not like well-drilled soldiers.

Other noise sources arise externally and can be eliminated if care is taken.

- Electrical interference: motors, ac power lines, and so on.
- Temperature fluctuations
- Vibrations that cause electrical components to shift

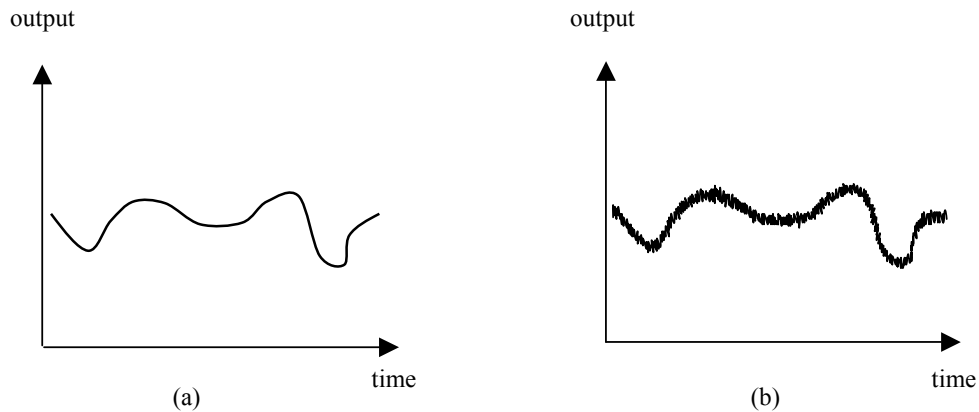


Figure 2.7 Noise is “clutter” that degrades signal fidelity: (a) with little noise; (b) with more noise [1]

Since noise is a random deviation from the average signal output, some convention is required to decide how to assign a single number to a given noise pattern. The usual definition is the root mean square (*rms*) deviation: the square root of the mean (average) of the square of the deviation as it varies in time.

Frequency Spectrum of Noise

Some noise components will appear at very specific frequencies. For example, a pump will vibrate a dewar a few times every second, and an ac power

line near a critical amplifier will introduce noise at the line rate – 50 cycles per second (Figure 2.8). The more fundamental noise sources will add some noise more or less uniformly at all frequencies. This is referred to as *white noise*, by analog to the fact that white light contains all wavelengths (frequencies) of light. Even if the noise is not quite white, it will generally contain a wide range of frequencies, and we can reduce the noise by eliminating unnecessary frequencies.

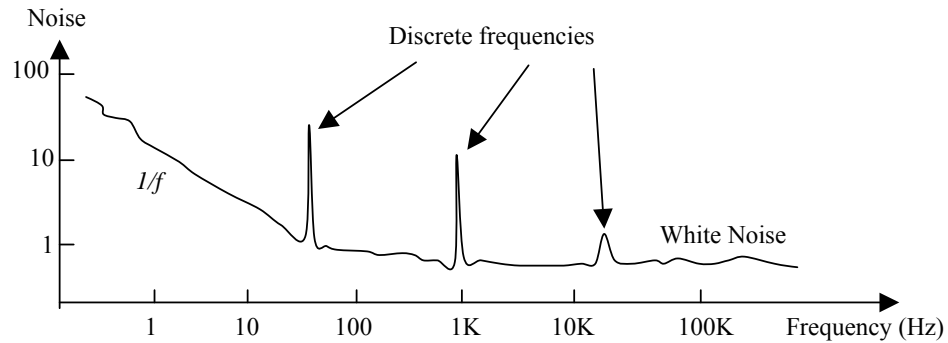


Figure 2.8 Frequency Spectrum of noise [1]

Noise Spectral Density

It can be shown that for white noises, the total noise voltage or current is proportional to the square root of the bandwidth. Even if the noise is not “pure white”, the square root of bandwidth rule is often used:

$$\text{“in-band” noise} \propto \sqrt{\Delta f} \quad 2.9$$

To compare the noise in various band-passes, we use the noise spectral density n . It is the noise N divided by square root of the band-pass Δf :

$$n = \frac{N}{\sqrt{\Delta f}} \quad 2.10$$

This is the noise spectral density, and it has unit of volts per root hertz ($V/H^{1/2}$). Its numerical value is the noise that would occur if the electrical band-pass were reduced to 1 Hz.

Signal to Noise Ratio

The signal-to-noise ratio (S/N) is the simple way to describe the cleanliness of a given signal level. It is simply the signal voltage divided by the *rms* noise voltage. An oscilloscope trace with an S/N ratio of 100 or more is a very clean pattern, with negligible noise. An S/N ratio of 10 is a little fuzzy, but the pattern is still clear. A ratio of 3 is pretty bad, and at 1 the signal is nearly lost (Figure 2.9).

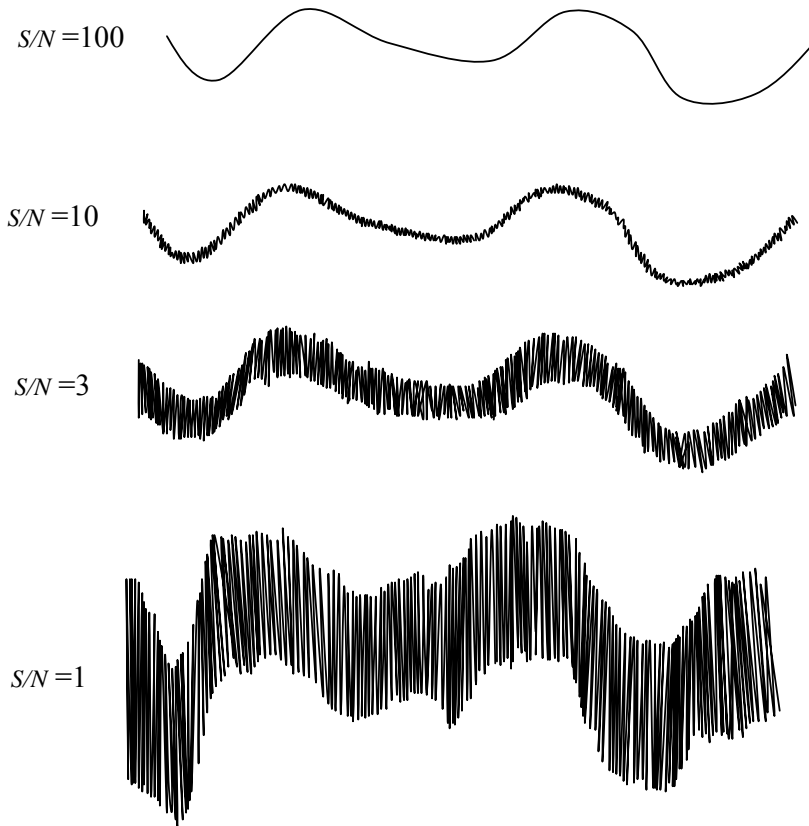


Figure 2.9 Detector output with varying signal-to-noise ratios [1]

S/N does not characterize the detector itself. We can get a better S/N for the same detector just by applying a higher incidence level. S/N does describe the conditions under which we were working. If we are trying to take data with an S/N ratio of 3, the results would not be trustable as much as if we had an S/N of 30, or better yet, 300.

Noise Equivalent Power

The noise equivalent power (*NEP*) is a measure of the ultimate sensitivity of a given detector, and it is a convenient number to use to estimate what the *S/N* ratio will be if the power available is known. *NEP* is the power that must fall on the detector to cause an *S/N* of 1.

NEP is determined by dividing the system noise by the responsivity (using the output per power input definition of responsivity).

$$NEP = \frac{\text{noise}}{\text{responsivity}} \quad (\text{Watts}) \quad 2.11$$

A variant uses the noise spectral density instead of the noise in the *NEP* formula. It is, then, *NEP* per unit bandwidth (*NEP'*).

$$NEP' = \frac{\text{noise spectral density}}{\text{responsivity}} = \frac{\text{noise}}{\sqrt{\Delta f} \times \text{responsivity}} \quad (\text{W/Hz}^{1/2}) \quad 2.12$$

Specific Detectivity

The *NEP* formula is convenient for predicting the minimum power, a given system can detect, but it has some undesirable features; (1) A good detector will have a small *NEP*, and (2) detectors of different sizes will have different *NEPs*, so we cannot say in general what a good *NEP* should be unless we specify the size of the detector.

The specific detectivity (D^*) (now normally just called detectivity or “*D-star*”) eliminates those two drawbacks. A large D^* is good, and for a given environment all good detectors should have the same D^* . The definition of D^* is;

$$D^* = \frac{\text{responsivity} \times \sqrt{\text{area}}}{\text{noise} / \sqrt{\Delta f}} = \frac{\mathfrak{R} \times \sqrt{A_d}}{N / \sqrt{\Delta f}} \quad 2.13$$

or,

$$D^* = \frac{\text{signal} \times \sqrt{\Delta f}}{\text{noise} \times \text{incidence} \times \sqrt{\text{area}}} = \frac{S\sqrt{\Delta f}}{NE\sqrt{A_d}} \quad 2.14$$

The units of D^* are $\text{cmHz}^{1/2}/\text{W}$. It is useful in predicting S/N in a given test environment.

$$S/N = D^* \frac{\text{incidence} \times \sqrt{A_d}}{\sqrt{\Delta f}} \quad 2.15$$

Linearity and Saturation

Detector outputs will increase linearly with input signal over some range of incidences, and fail to be linear at some large incidences (Figure 2.10).

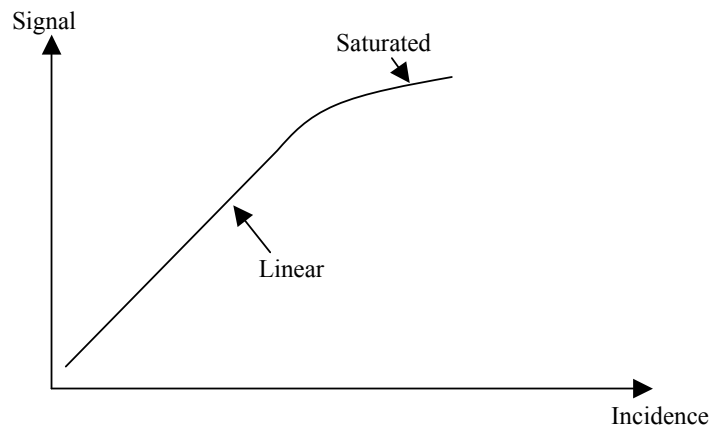


Figure 2.10 Signal vs Incidence plot showing linear and saturated regions [1]

A major source of deviation from linearity is the saturation of the detector or electronic circuit. That is, as the incidence and the signal increase, some physical constraint is reached, and the signal cannot continue to increase. This could be due to the electrical breakdown of the detector itself, or some electronic components.

More generally, there is an amplifier in the circuit that will put out only a limited voltage.

Dynamic Range

The dynamic range is the ratio of the highest useful signal to the lowest measurable signal. Highest useful signal might be defined as the point at which linearity specification is exceeded, and lowest measurable signal might be the signal at which $S/N=1$.

Frequency Response

The detector or system (detector plus electronics) will generally respond equally well to a range of frequencies, but will not respond as well to higher frequencies. The frequency response is described by a plot of responsivity versus frequency curve (Figure 2.11). It can also be described by providing the corner frequency, in which case one implies that frequency response curve obeys an equation of the form

$$S = S_o \frac{1}{\left[1 + \left(\frac{f}{f_c}\right)^2\right]^{1/2}} \quad 2.16$$

where f_c is the corner frequency, and S_o is the signal at low frequencies.

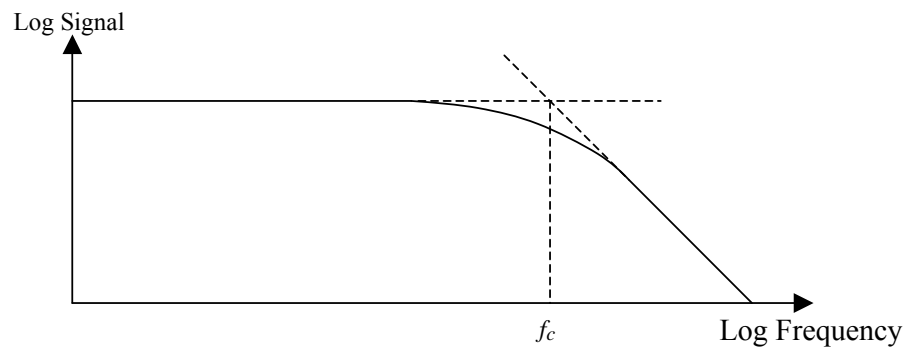


Figure 2.11 Frequency response [1]

Spatial Considerations

Uniformity of Response: No detector is perfectly uniform in terms of responsivity over its surface. Some parts of the detector are more sensitive than others. A response profile (a plot of responsivity versus position) is a way to report the uniformity.

Modulation Transfer Function (MTF): *MTF* is sometimes called the spatial equivalent of the frequency response of a detector, or the spatial frequency response. It is a measure of how well the detector can sense small details. *MTF* depends on detector size and the uniformity of response across the detector. A small detector with uniform response will have better *MTF* and be able to see smaller features than will a large one, or one with response that tapers off near the detector edges.

Crosstalk

If one has an array of detectors and images a spot on one detector, there should be no signal from the other detectors. In practice, some signal will be present on the others, although it should be very small. This excess signal is said to be due to crosstalk. Crosstalk is generally measured as a percentage of the input or driving signal. A requirement that crosstalk be less than 5% would be easy to meet, and a requirement of 0.05 % would be very hard to meet.

Crosstalk can be due to optical effects (e.g. reflections from the detector on which the spot was focused) and electrical effects (e.g. capacitance between the signal leads) as illustrated in Figure 2.12.

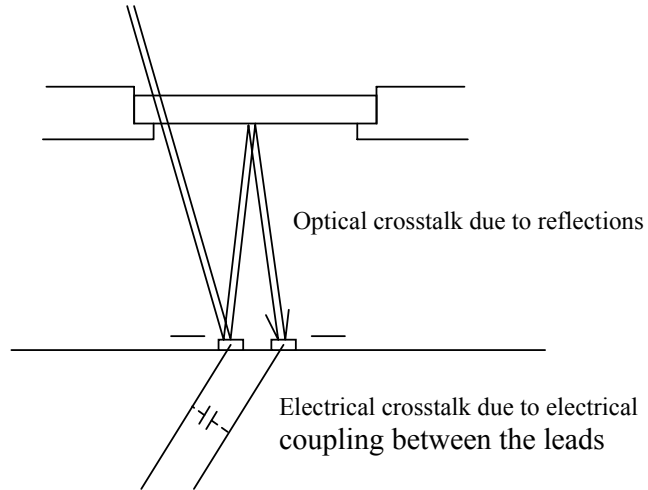


Figure 2.12 Crosstalk due to optical reflections and electrical coupling [1]

2.5 Materials for Infrared Detectors

InSb has been an important semiconductor for infrared detector applications in the 3-5 μm atmospheric window, and there has been significant interest in large area InSb focal plane arrays (FPAs). InSb offers important advantages over HgCdTe, the other widely used infrared material, such as relatively easy large area homogeneous growth and stronger covalent bonding. However, InSb detectors can sense only in the MWIR region. Due to the difficulties in epitaxial growth and processing steps of HgCdTe, a number of III-V semiconductor structures such as InAsSb [11-20][22], InSbBi [29-30][23], InAsBi [31], InAsSbBi [31-32], GaInSbBi [34], InTlSb, [35-40], InTlP [41], and InTlAs [41], have been investigated as an alternative for LWIR photodetectors. In spite of the encouraging results of InTlSb and InAsSb LWIR photodetectors, further reduction of band gap energy is necessary for the high-performance detector operation. In addition to these III-V structures, some heterostructures, such as AlInSb/InAsSb/AlInSb [21][23], are also of interest in infrared detector applications.

Kim *et al.* [11] reported LP-MOCVD grown $p^+ \text{-InSb}/\pi\text{-InAs}_{0.15}\text{Sb}_{0.85}/n^+ \text{-InSb}$ heterojunction photodiodes on (100) semi-insulating GaAs substrate in the 8-

13 μm infrared region near 300K. The cut-off wavelength of the device was 13 μm , and they reported a voltage responsivity-area product of $3 \times 10^{-5} \text{ V cm}^2/\text{W}$ at 300 K for 10.6 μm [11]. In the later studies, Kim *et al.* [12] also reported the room temperature operating photoconductors based on p-InAs_{0.23}Sb_{0.77}/p-InSb grown on (100) semi-insulating GaAs substrates by LP-MOCVD. They measured the hole and electron mobilities of 923 cm^2/Vs and 36000 cm^2/Vs respectively by Hall Effect. The geometry of the fabricated photoconductive diode was $4 \times 3 \text{ mm}^2$. The spectral photoresponse measurements were carried out by FTIR spectrometer at temperatures between 77 and 300 K. Kim *et al.* [12] reached a peak responsivity of 4 mV/W at 8 μm and at 300 K for 1 V bias. 14 μm cut-off wavelength was observed at 300 K. The corresponding Johnson noise limited detectivity of the photoconductor was estimated to be $\approx 3.27 \times 10^7 \text{ cm Hz}^{1/2}/\text{W}$ at 300 K.

Rakovska *et al.* [13] and Marcadet *et al.* [14] presented MBE grown InAs_{0.91}Sb_{0.09} p-i-n photovoltaic mid-infrared detector grown on GaSb substrate operating at room temperature. The photovoltaic detector consisted of a 1.2 μm -deep $100 \times 100 \text{ }\mu\text{m}^2$ mesa obtained by ion beam etching [13]. From I-V characterization, Rakovska *et al.* [13] obtained R_0A values of $1.05 \text{ }\Omega\text{cm}^2$ at 250K and $0.12 \text{ }\Omega\text{cm}^2$ at 295K. The resulting detectivity was $4.5 \times 10^9 \text{ cm Hz}^{1/2}/\text{W}$ at 250K and 3.39 μm [13][14]. According to authors, the design can be improved by increasing the gap of the corresponding n-doped barrier [13]. In another publication, Rakovska *et al.* [22] obtained a detectivity value of $7 \times 10^9 \text{ cm Hz}^{1/2}/\text{W}$ at 250K. This led to an *NETD* value of lower than 80mK.

Dobbelaere *et al.* [15] reported on the first InAs_{0.85}Sb_{0.15} infrared photodiodes, grown on GaAs and GaAs-coated Si substrates by molecular beam epitaxy. The photodiodes were fabricated by etching mesas with a height of 2.5 μm and an area of $1.25 \times 10^{-4} \text{ cm}^2$ in a 5:1 Lactic acid: nitric acid etching solution. The measured R_0A products for InAs_{0.85}Sb_{0.15} on GaAs and InAs_{0.85}Sb_{0.15} on GaAs-coated Si were $192 \text{ }\Omega \text{ cm}^2$ and $42 \text{ }\Omega \text{ cm}^2$ respectively. The cut-off wavelength of the photodiode is about 4.6 μm and the peak responsivity was 1.25 A/W at 3.8 μm

with quantum efficiency of 41%. The maximum values of the detectivity for InAs_{0.85}Sb_{0.15} on GaAs and InAs_{0.85}Sb_{0.15} on GaAs-coated Si were 1.5×10^{11} cm Hz^{1/2}/W and 5.0×10^{10} cm Hz^{1/2}/W, respectively at 3.8 μm and 77K.

Beşikçi *et al.* [16] made a comparative study on the p-i-n InAs_{0.8}Sb_{0.2} detectors grown on GaAs substrate by molecular beam epitaxy. The fabricated diode had an area of 50x200 μm² and the peak detectivity was 1.4×10^{10} cm Hz^{1/2}/W at 3.9 μm. The peak detectivity at 240K was 7.5×10^8 cm Hz^{1/2}/W at 4.7 μm and the cut-off wavelengths of the detector at 80K and 240K were 4.7 μm and 5.4 μm respectively.

Bethea *et al.* [17] fabricated InAs_{0.02}Sb_{0.98} detectors on semi-insulating GaAs substrate by molecular beam epitaxy and measured the optical characteristics of the detectors. They fabricated the detector by cleaving a bar of 1x3 mm² and contacting the InAs_{1-x}Sb_x layer using Indium. The noise voltage was measured to be quite low being only 7 nV. This corresponded to a noise current of $i_n = 4$ pA since the device resistance was 1.7 kΩ at 77K. The detectivity was 3×10^{10} cm Hz^{1/2}/W at 5.4 μm. In addition, 47% internal quantum efficiency was achieved at 5.4 μm. In a later publication, Bethea *et al.* [18] also reported MBE grown InAs_{0.22}Sb_{0.78} on semi-insulating GaAs substrate, and the fabrication and characterization of photoconductive detectors. 4x2 mm² detectors were fabricated in order to measure the photoconductance response. The measured responsivity of the detector was 1.5×10^{-2} V/W, which corresponded to a detectivity of 10^8 cm Hz^{1/2}/W at 8 μm for V= 9V at a temperature of 77K. The cut-off wavelength was measured to be 10.5 μm. Hall effect measurements were also performed and the electron mobility was found to be 12650 cm²/(Vs) at 77K.

Mohammed *et al.* [19] reported the operation of broadband InAs_{0.85}Sb_{0.15} p-n junction photodetectors grown on InAs substrate by liquid phase epitaxy. They achieved a 70K detectivity of 1.5×10^{11} cm Hz^{1/2}/W and 200K detectivity of 2×10^{10} cm Hz^{1/2}/W at 3.5 μm, and peak external quantum efficiency of 40%.

Kim *et al.* [20] studied the growth and characterization of InAs_{0.05}Sb_{0.95} alloys on GaAs and Si substrates for uncooled infrared detector applications. Photovoltaic and photoconductive devices were grown on (100) GaAs and Si substrates, respectively, by MBE. The structure for the photovoltaic detectors grown on (100) GaAs substrates consisted of top n⁺- InAs_{0.05}Sb_{0.95} (0.35 μm, 3x10¹⁷ cm⁻³), middle p- InAs_{0.05}Sb_{0.95} (3 μm, 1x10¹⁷ cm⁻³), and bottom p⁺- InAs_{0.05}Sb_{0.95} (2 μm, 3x10¹⁷ cm⁻³) layers. The cut-off wavelength of the photovoltaic detector was 7.5 μm and the Johnson noise limited detectivity was estimated to be 4.2x10⁷ cm Hz^{1/2}/W at 300K.

Wojkowski *et al.* [21] presented the first demonstration of InAsSb/AlInSb double heterostructure detectors for room temperature operation in the 5-8 μm wavelength range. The photovoltaic detectors, grown by MBE, consisted of p⁺- Al_{0.07}In_{0.93}Sb / π-InAs_{0.06}Sb_{0.94} / n⁺-Al_{0.07}In_{0.93}Sb double heterostructure on (100) GaAs substrate. The 400x400 μm² mesa structures with Ti/Au contacts were fabricated using standard photolithography, etching, and metallization techniques. No optical immersion or surface passivation was used. The Johnson noise limited detectivity of the devices at room temperature was calculated as ~2x10⁸ cm Hz^{1/2}/W which is comparable to MCT detectors at the same wavelength. The authors found the detector quantum efficiency as 40%. The authors proposed three main ways to improve the performance of the photodetectors. First, recombination can be suppressed via the optimization of the material parameters. Specifically, π-doping of the active region has been shown to minimize the Auger recombination in room temperature detectors. Secondly, optical immersion can be used to increase the optical area of detection. This can lead to seven-fold increase in the response. Finally, surface passivation can be used to decrease the number of available surface states that can degrade detector performance [21]. Kudo and Mishima [23] obtained 24750 cm²/Vs electron mobility for Al_{0.15}In_{0.85}Sb/InAs_{0.124}Sb_{0.876}/ Al_{0.15}In_{0.85}Sb heterostructures at room temperature.

Tevke *et al.* [24] reported the characteristics and dark current analysis of InSb p-i-n photodetectors grown on GaAs coated Si substrates by MBE. Mesa structures with areas of $400 \times 80 \mu\text{m}^2$ and $400 \times 400 \mu\text{m}^2$ were defined by standard photolithography, wet chemical etching and, metallization. The zero bias differential resistance (R_0) at 77K for $400 \times 80 \mu\text{m}^2$ mesa structure was around 8.3 k Ω and the dark current was measured to be 13 μA under 0.1 V reverse bias. The voltage responsivity for $400 \times 80 \mu\text{m}^2$ mesa structure was $1.2 \times 10^4 \text{ V/W}$ at 77K, and the cut-off wavelength was around 5.5 μm . The current responsivity and quantum efficiency were around 1.4 A/W and 40%, respectively. Michel *et al.* [25] made a study on InSb infrared photodetectors based on p-i-n structures grown heteroepitaxially on GaAs coated Si. The peak voltage responsivity of $400 \times 400 \mu\text{m}^2$ mesa structures was 1000 V/W at around 4 μm and the Johnson-noise-limited detectivity of $2.8 \times 10^{10} \text{ cm Hz}^{1/2}/\text{W}$ was typically obtained for these devices at 77K.

Kepten *et al.* [26-27] presented the InSb monolithic infrared focal plane array where photodiodes and field effect transistors were integrated. The photodiode was connected directly to the integrating capacitor while the transistor controls the integrated signal-charge transfer to the video line. The measured responsivity of the system ($R_i(\lambda)$) at 3.83 μm was 2.25 A/W, and the effective quantum efficiency was 0.73. The measured noise current spectral density was equal to 1.72 pAHz^{-1/2}. Accordingly, the detectivity at 3.83 μm was calculated to give $1.28 \times 10^{11} \text{ cm Hz}^{1/2}/\text{W}$, and the noise equivalent temperature difference (NETD) of the system was estimated to be 39 mK [26-27].

Elliot [28] studied the epitaxially grown $\text{p}^+ \text{-InSb}/\text{p}^+ \text{-InAlSb}/\pi \text{-InSb}/\text{n}^+ \text{-InSb}$ devices on InSb substrate operated at room temperature. At ambient temperature (294K) the detectivity of the device was $2.5 \times 10^9 \text{ cm Hz}^{1/2}/\text{W}$, with a peak wavelength of $\sim 6 \mu\text{m}$.

Lee *et al.* [29] reported the LP-MOCVD growth and characterization of InSbBi epitaxial layers with the energy bandgap as low as 0.13 eV ($\sim 9.3 \mu\text{m}$) at

77K. A cut-off wavelength of 9.3 μm at 77K was observed corresponding to about 5.8% of Bi incorporation in InSbBi layers. This is an encouraging result for the use of Bi-containing III-V alloys in the development of the LWIR detector operating in the 8-12 μm atmospheric window [29]. In a later study, Lee *et al.* [30] demonstrated the operation of InSb_{0.96}Bi_{0.04} infrared photoconductive detectors grown by low-pressure metal organic chemical vapor deposition on semi-insulating GaAs substrates. The fabricated detector showed a cut-off wavelength of 7.7 μm at 77K. The responsivity of the InSb_{0.96}Bi_{0.04} photodetector at 7 μm was about 3.2 V/W at 77K. The corresponding Johnson-noise limited detectivity was $4.7 \times 10^8 \text{ cmHz}^{1/2}/\text{W}$. Ma *et al.* [31], Huang *et al.* [32], and Noreika *et al.* [33] proposed InSbBi/InSb, InAs_{1-x}Bi_x and InAs_{1-x-y}Sb_yBi_x materials for use in fabrication of p-n junction infrared detectors operating in the 8-12 μm atmospheric window.

The growth of a new quaternary semiconductor alloy GaInSbBi suitable for 8-12 μm infrared detector applications by molecular beam epitaxy was reported for the first time by Du *et al.* [34]. The cut-off wavelength of Ga_{0.04}In_{0.96}Sb_{0.97}Bi_{0.03} on InP substrate was measured to be 10.7 μm at 77K.

Choi *et al.* [35][36], Lee and Razeghi [37], and Van Schilfgaarde *et al.* [38] reported the growth and optical properties of In_{1-x}Tl_xSb/InSb heterostructures on GaAs substrates for LWIR applications. Staveteig *et al.* [39] presented infrared photoconductors based on InTlSb/InSb grown by LP-MOCVD on semi-insulating GaAs substrates. The cut-off wavelength of InTlSb was measured to be 8 μm at 77K while it is 5.5 μm for InSb at the same temperature. The specific detectivity was estimated to be $3 \times 10^8 \text{ cmHz}^{1/2}/\text{W}$ at 7 μm at 77K. Kim *et al.* [40] studied on long-wavelength InTlSb photodetectors operating at room temperature. The InTlSb photodetectors were grown directly on (100) semi-insulating GaAs substrates by LP-MOCVD. Photoresponse up to 11 μm at room temperature was observed. The maximum responsivity of the In_{0.96}Tl_{0.04}Sb photodetectors was about 6.64 V/W at 77K, corresponding to a detectivity of about $7.64 \times 10^8 \text{ cmHz}^{1/2}/\text{W}$. The voltage responsivity and detectivity of In_{1-x}Tl_xSb photodetectors are listed in Table 2.1. Van

Schilfgaard *et al.* [41] offered that $\text{In}_{1-x}\text{Tl}_x\text{P}$ and $\text{In}_{1-x}\text{Tl}_x\text{As}$ form suitable materials for infrared detectors. $\text{In}_{0.33}\text{Tl}_{0.67}\text{P}$ and $\text{In}_{0.85}\text{Tl}_{0.15}\text{As}$, which were estimated to have a gap of 0.1 eV, were studied. Their binding energies are larger than that of InSb, and they are found to form stable zinc-blende alloys for all values of x . $\text{In}_{1-x}\text{Tl}_x\text{P}$ nearly lattice matches to InP, and offers the potential to monolithically integrate detector array and read-out circuit [41].

Table 2.1: The performance of the $\text{In}_{1-x}\text{Tl}_x\text{Sb}$ photodetectors at 77K [40].

$\text{In}_{1-x}\text{Tl}_x\text{Sb}$ x value	λ_c (μm)	R_v (V/W)	D^* (10^8 $\text{cmHz}^{1/2}/\text{W}$)	μ ($10^3 \text{ cm}^2/\text{Vs}$)	τ (ns)
0.02	6.5	2.73	2.47	1.29	19.2
0.04	7.3	3.64	7.64	2.00	50.1
0.05	8.4	3.56	8.54	2.75	40.4
0.06	9.4	0.79	2.63	4.13	10.3

2.6 Thermal Imaging

There are two basic types of infrared imaging systems: mechanical scanning systems and staring systems.

A mechanical scanner utilizes one or more moving mirrors to sample the object plane sequentially in a row-wise manner and project these onto the detector. The advantage is that only one single detector is needed. The drawbacks are that high precision and thus expensive opto-mechanical parts are needed, and the detector response time has to be short. As mentioned above, detector arrays are also used for this application. For example, a long linear detector array can be used to simultaneously sample one column of the object plane. By using a single moving mirror, the whole focal plane can be sampled. In contrast, when a single detector is

used, two mirrors moving in two orthogonal directions must be used, one of them moving at high speed, the other one at lower speed.

Detector arrays operated as focal plane arrays (FPA) (or staring arrays) are located in the focal plane of a camera system, and are thus replacing the film of a conventional camera for visible light. The main advantage is that no moving mechanical parts are needed. The drawback is that the detector array is more complicated to fabricate. However, with the ascent of rational methods for semiconductor fabrication, economy will be advantageous, if the production volumes are large. The general trend is that infrared camera systems will be based on FPAs, except for special applications.

The spatial resolution of the image is determined by the number of pixels of the detector array. Common formats for commercial infrared detectors are 320x240 pixels (320 columns, 240 rows), and 640x480. The latter format, which is nearly the resolution obtained by standard TV, is commercially available.

Detector arrays are more complicated to fabricate, since besides the detector elements with the function of responding to radiation, electronic circuitry is needed to multiplex all the detector signals to one or a few output leads in a serial manner. The output from the array is either in analogue or digital form. In the former case analogue to digital conversion is usually done external to the detector array. The electronic chip used to multiplex or read out the signals from the detector elements are usually called simply readout integrated circuit (ROIC) or (analogue) multiplexer.

The ROIC is usually made using silicon CCD (charge coupled device) or CMOS technology. However, the detector elements must often be fabricated from more exotic materials as discussed above. The exceptions are e.g. platinum silicide or micro-bolometers, which can be based on silicon technology. In the former case, a hybrid approach is most common, in which case all the detector pixels are fabricated from a separate detector chip. This detector chip is then flip-chip bonded

to the ROIC chip. Flip-chip bonding involves the processing of metal bumps onto contact holes, one per pixel, of both the detector chip and the ROIC. Using special equipment, the two chips are first aligned to each other. Then the chips are put in contact, while applying heat and/or mechanical force. During this process, the two chips become electrically connected to each other via the metal bumps. Usually indium is used for the bumps due to its excellent low temperature properties.

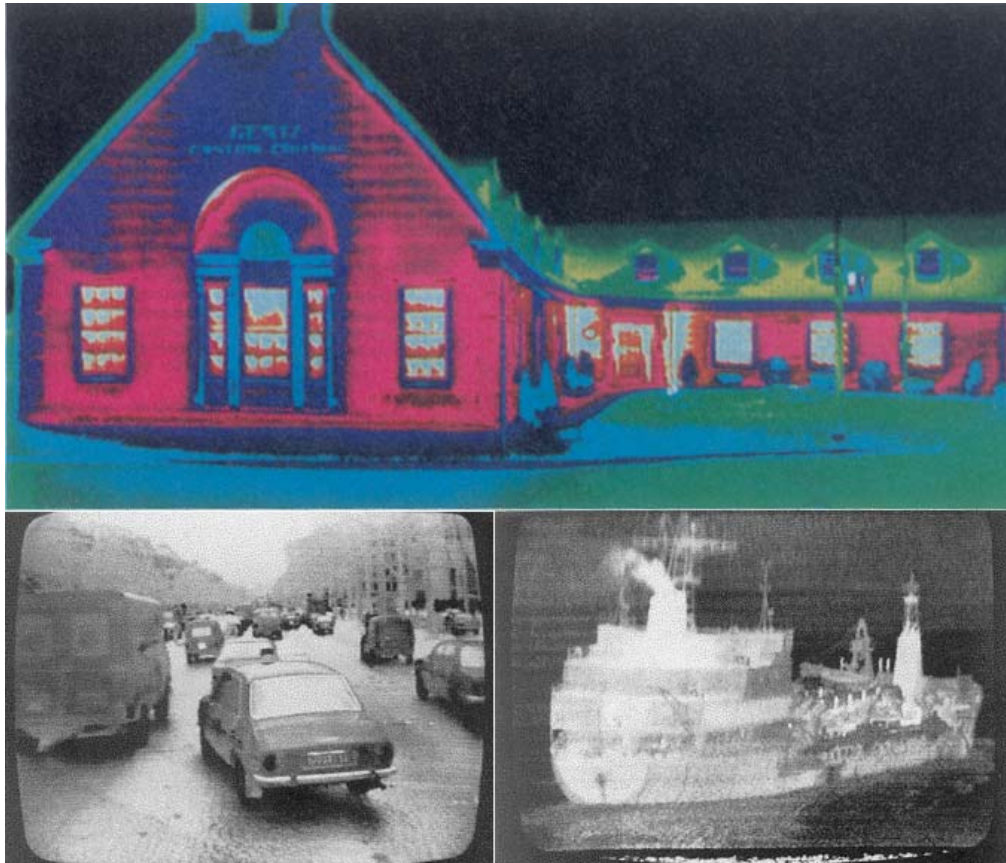


Figure 2.12. Three infrared images taken by different infrared imagers [1]

Uniformity of the detector elements across the array is an important issue for obtaining high performance. In fact, individual pixel response characteristics differ considerably across an array in most cases. Therefore, so-called pixel correction has to be done prior to the presentation of the final image. This amounts to calibrating each individual pixel, by exposing the array to calibrated surfaces of known temperature.

CHAPTER III

TEST DETECTOR FABRICATION AND CHARACTERIZATION

The description of semiconductors used in this study, the design of masks, which are necessary for processing of photodiodes and fabrication and characterization of test diodes are discussed in this chapter.

3.1 Semiconductor Structures Used for Detector Fabrication

In an infrared imager, the detector properties strongly depend on the semiconductor material system. For the device active layer, a material with an appropriate bandgap is chosen in order to absorb photons in the wavelength range of interest. The maximum wavelength a material will absorb is determined by its bandgap energy (E_g) which is the energy difference between the bottom of the conduction band and the top of the valence band

For the 3-5 μm window, the most widely used materials are narrow bandgap semiconductors such as InSb and HgCdTe. These types of detectors use interband absorption as detection process. Due to their narrow bandgap property, the number of thermally generated carriers at room temperature is so high that these detectors have to be cooled down to liquid nitrogen temperature (77 K). Although this

cooling process increases the cost of detector systems, because of high responsivity of narrow bandgap semiconductor photodetectors, most of the infrared imagers use these detectors.

InSb is a well-established material for high quality thermal imaging in the 3-5 μm wavelength range. With the lowest bandgap of any binary III-V semiconductor material, it exhibits very low electron effective mass ($0.014m_0$ at 300K) and high mobility ($8 \times 10^4 \text{ cm}^2\text{V}^{-1}\text{s}^{-1}$). It is a direct bandgap semiconductor with 0.17 eV bandgap (at 300 K). The following figure shows the E-k plot of InSb.

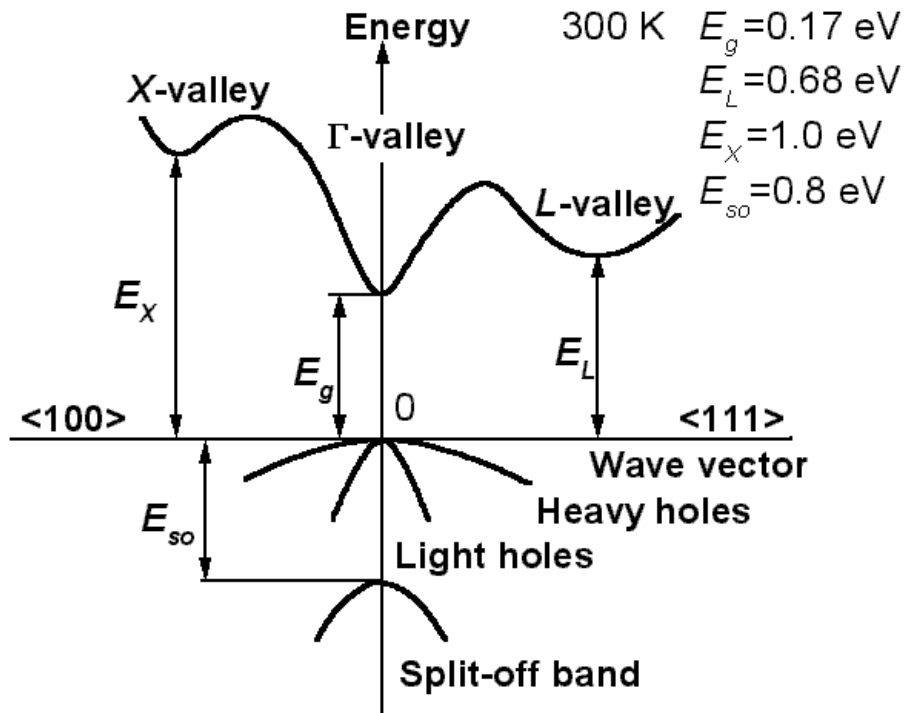


Figure 3.1 E-k diagram of InSb

While not widely used, AlInSb can be used as a barrier material for mid-IR interband cascade laser and other antimonide device structures [42]. In this study, a three-layer $P^+\pi n^+$ AlInSb/InSb/InSb structure is used. The capital letter denotes the large band gap material, which is AlInSb, in the structure and the plus symbol

indicates high doping density. π means that the unintentional doping of the middle (active) layer is near intrinsic p. Figure 3.2 shows the energy band diagram of AlInSb/InSb/InSb heterojunction.

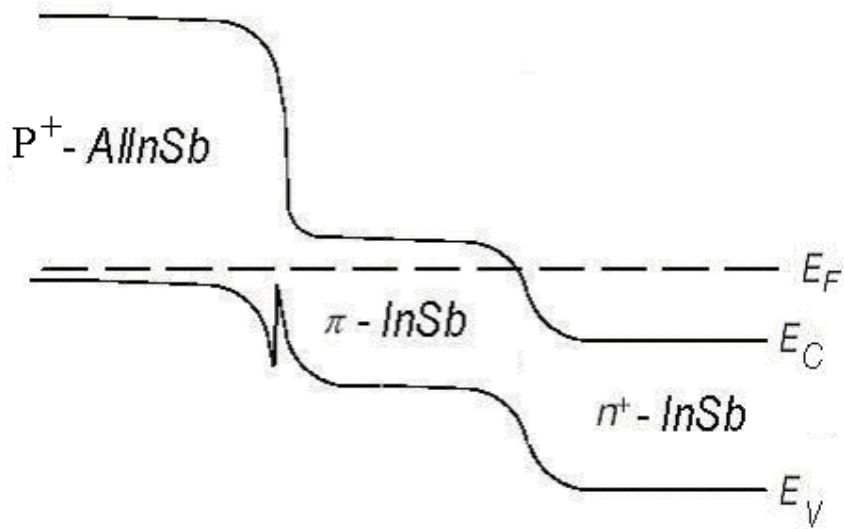


Figure 3.2 Energy band diagram of AlInSb/InSb/InSb heterojunction

The semiconductor structures used in this study is p^+ InSb/intrinsic InSb/ n^+ InSb grown on GaAs coated Si substrate and p^+ $Al_{0.1}In_{0.9}Sb$ /intrinsic InSb/ n^+ InSb grown on GaAs coated Si substrate as shown in figure 3.3. Both wafers were grown by molecular beam epitaxy (MBE) at Northwestern University, USA.

p^+ $Al_{0.1}In_{0.9}Sb$ ($1\mu m$)	p^+ InSb ($1\mu m$)
intrinsic InSb ($6\mu m$)	intrinsic InSb ($6\mu m$)
n^+ InSb ($1\mu m$)	n^+ InSb ($1.5\mu m$)
GaAs Buffer ($2\mu m$)	GaAs Buffer ($2\mu m$)
Si Substrate	Si Substrate
(a)	(b)

Figure 3.3 Semiconductor wafer structures used in this study (a) AlInSb/InSb heterojunction on Si substrate (b) InSb homojunction on Si substrate.

The investigation of the characteristics of the homojunction structure shown in Fig. 3.3 (b) was performed by Selcuk Ozer as a part of his Ph.D. study at the Electrical and Electronics Engineering Department of METU. Some of his results will be presented here in order to allow the comparison of the two structures and see the effects of the larger bandgap AlInSb on the detector performance.

3.2 Fabrication of Test Detectors

Before the fabrication of the test detectors, the test detector masks are designed to perform test detector process in order to evaluate the detector performance. This mask set contains etching, passivation and metallization masks.

The design and fabrication of 128x128 array masks and the test detector masks were followed by the fabrication process. The fabrication processes were optimized before starting the fabrication.

The following processes are done in the detector fabrication.

- Photoresist Spinning
- Photolithography
- Etching
- Passivation Coating
- Metallization and Lift-off
- Metal Etching
- Electroplating
- Reflow
- Dicing
- Flip-Chip Bonding

The detailed information about these processes is given below.

Photoresist Spinning

Photoresist (PR) is a photon sensitive organic material that can be used in microelectronic technology. Photoresist spinning is an important stage, which is performed in all detector fabrication steps. Two kinds of photoresist can be used in this process: positive photoresist or negative photoresist. Positive PR needs to be baked at a certain temperature after spinning. The exposed regions of the positive PR will be solvable in a solution called “Developer”. Therefore, the pattern in the mask will be transformed to the sample, and the sample will be ready for the following process. The exposed regions of the negative photoresist will become resistant to solvents and the unexposed regions will be removed by the developer. So, the type of the PR, which will be used in the processes, must be known while designing the masks. Therefore, the type of the mask is determined by the process and the type of the PR used in the process. In table 3.1, the type of the masks is given according to etching and lift-off processes for both PR types. The designed masks will be printed on a glass or quartz by Cr plating and the patterns in the mask are defined by this Cr plating. In table 3.1, “**dark**” represents the Cr plated regions and “**transparent**” represents the non-plated regions of the glass mask.

Table 3.1 Mask types according to process to be done and photoresist used

PROCESS	PHOTORESIST TYPE	TYPE OF THE MASK TO BE DESIGNED
ETCHING	POSITIVE PR	POSITIVE MASK (the etched regions on the substrate should be transparent on the mask)
	NEGATIVE PR	NEGATIVE MASK (the etched regions on the substrate should be dark on the mask)
LIFT-OFF	POSITIVE PR	NEGATIVE MASK (the metal deposited regions on the substrate should be transparent on the mask)
	NEGATIVE PR	POSITIVE MASK (the metal deposited regions on the substrate should be dark on the mask)

The fabrication masks are designed according to positive PR and the following processes are explained according to positive PR usage. The photoresist is coated on the sample by spin coating method. In this method, the sample is placed on the chuck of the spinner and it is fixed by the vacuum hole on the chuck. Then the chuck is rotated by a certain angular speed and the PR is dropped on the sample. The PR will spread on the sample uniformly due to the force created by the rotation. Finally, the PR coated sample will be baked in an oven at a certain temperature and the PR coating step is finished (Figure 3.4).



Figure 3.4 Semiconductor substrate coated by photoresist

Photolithography

Lithography is the process of transferring geometric shapes on the mask to the surface of the semiconductor wafer. These shapes make up the parts of the detectors, such as the mesa, contact windows, metal interconnections, and so on.

The PR coated sample and the corresponding process mask are aligned by using a “Mask Aligner”. After the alignment, the sample is exposed to ultraviolet light from the backside of the mask (Figure 3.5a). The exposed regions of the PR are developed and the sample is cleaned by de-ionized water (DIW). Finally, the sample is hard baked and the pattern in the mask is transformed to the sample (Figure 3.5b)

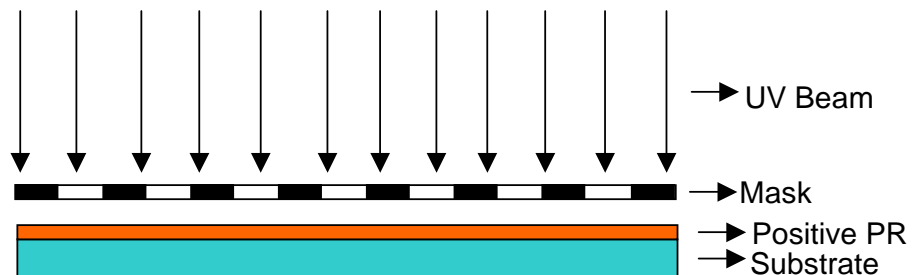


Figure 3.5a Photolithography

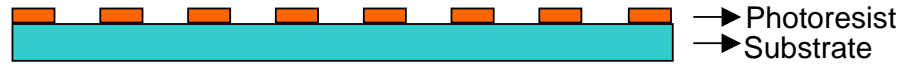


Figure 3.5b Developed Photoresist

Etching

Resist patterns defined by the lithographic techniques described above are not permanent elements of the final device but only replicas of detector features. To produce detector features, these resist patterns must be transferred into layers comprising the device. One method of transferring the patterns is to selectively remove the unmasked portions of a layer, a process generally known as etching [43]. Two types of etching techniques are used in microelectronic technology: Dry etch and wet-chemical etch. Dry etching is synonymous with plasma-assisted etching, which denotes several techniques that use plasmas in the form of low-pressure gaseous discharge [43].

There is no exclusively physical dissolution process for the most materials that transfer molecules or atoms out of the solid into the liquid phase. Wet etching in most cases is only possible if the dissolution is accompanied by a chemical change of the material. Several kinds of wet etching methods are available: Etching by acid-base reactions, non-oxidizing etching by forming complexes, oxidative etching, and enzymatic etching process [44]. In this study, the method used to remove the unnecessary parts of the semiconductor samples is like the oxidative etching. The etching solution generally contains both the oxidizer and a solvent, and the oxidized species and reactants are preferably rapidly soluble materials. The oxidizing agent (solution) oxidizes the semiconductor surface and the reactant removes the oxide layer from the surface of the semiconductor.

The most important parameter in optimizing this process is the etch rate of the solution. The mixture ratio of the solution, the stir rate, and the temperature are all arranged to have a controllable etch rate. The citric acid - hydrogen peroxide solution is used to etch the InSb based materials for better control of lateral versus

vertical etch rate, for improved uniformity. Figure 3.6 shows the sample after etching and PR removal by extra pure acetone.



Figure 3.6a Etched Substrate



Figure 3.6b Photoresist removed after etching

Passivation Coating

After etching, the photodiodes must be coated by a passivation material in order to protect them and to reduce the surface leakage (Figure 3.7). Two ways of coating process can be carried out to passivate the detector: Deposition and spin coating. The whole sample is coated by the passivation material and using the corresponding mask the contact places is opened by removing the passivation with a proper solution. Finally, hard bake is performed to harden the passivation material.

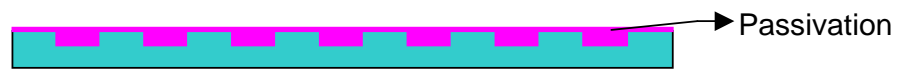


Figure 3.7a Passivation coated substrate

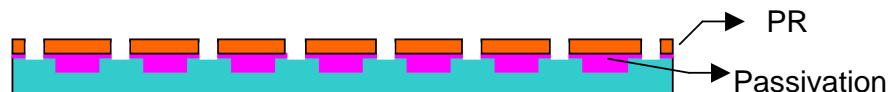


Figure 3.7b PR is developed and passivation openings are formed

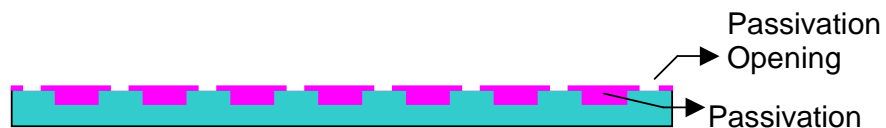


Figure 3.7c Passivated substrate except for top of the diodes

Metallization and Lift-off

Metallization is a thin film growth process. One of these processes is thermal evaporation, which is used to deposit metal on the semiconductors in this study. Evaporation involves local heating of a target material to a sufficiently high temperature with vapor partial pressure larger than chamber pressure (typically at 0.1-1 torr) to condense on substrate. Many materials, such as Al, Si, Ti, Mo, glass, Cr, Ag, can be evaporated by this method. Evaporation of target materials can be done by resistive heating or high-energy electron-beam bombardment. Resistive heating is in solid phase, so the container can cause contamination. However, e-beam is focused to the target and so it is cleaner but can cause x-ray radiation, and the equipment is more complex.

Lift-off is a process of removing the unwanted metals from the sample. Firstly, photolithography is done after coating PR to the substrate and the pattern is obtained. Then, metal is deposited on the whole sample (Figure 3.8b) and finally, the photoresist is removed with the metal deposited on it by acetone (Figure 3.8c). Therefore, the necessary metal contacts are obtained from the terminals of the devices.

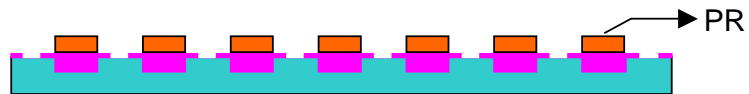


Figure 3.8a Developed PR for metal deposition

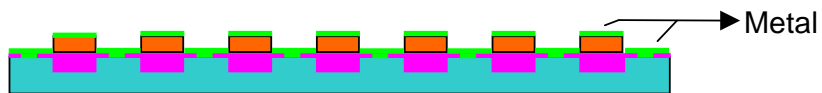


Figure 3.8b Deposited Metal

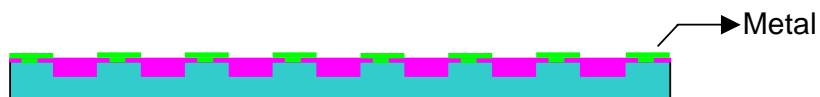


Figure 3.8c The unnecessary metal layers are removed by lift-off

Metal Etching

The unnecessary metal layers on the substrate can be removed by “Reactive Ion Etcher (RIE)” using suitable plasma such as, O_2 , N_2 , Ar, SF_4 , and CF_4 . Another way for removing metals from the substrate is the wet etching. Using a proper solution the unwanted metal layers can be removed.

Electroplating

Electroplating is the deposition of a metallic coating onto an object by putting a negative charge onto the object and immersing it into a solution which contains a salt of the metal to be deposited. The metallic ions of the salt carry a positive charge and are attracted to the part. When they reach it, the negatively charged part provides the electrons to reduce the positively charged ions to metallic form.

The tops of the mesa structures are plated by Indium in order to have a solder connection with the read-out integrated circuit. As the diodes are individual in the array, the electrical connection must be satisfied between all parts to be plated. This electrical connection can be done by deposition a thin metal layer on the whole sample. After preparing the corresponding plating solution, the sample is connected to the cathode of the plating circuit as shown in figure 3.9. Then, the plating process starts by applying enough current to the circuit.

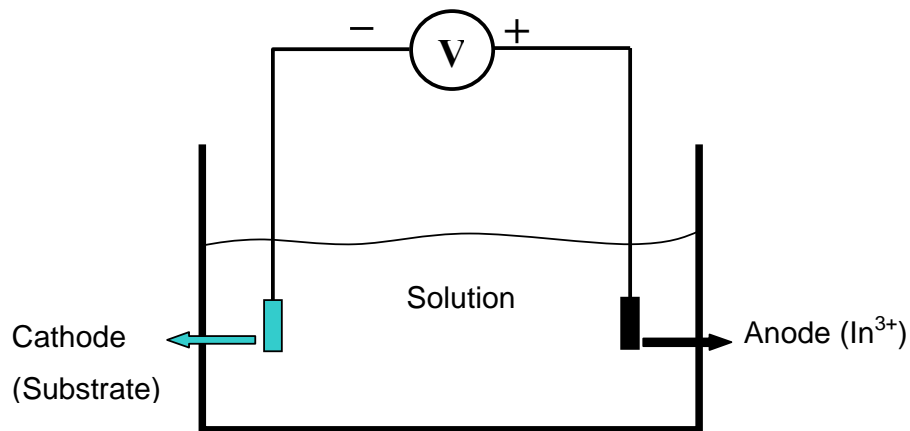


Figure 3.9 The setup for electroplating

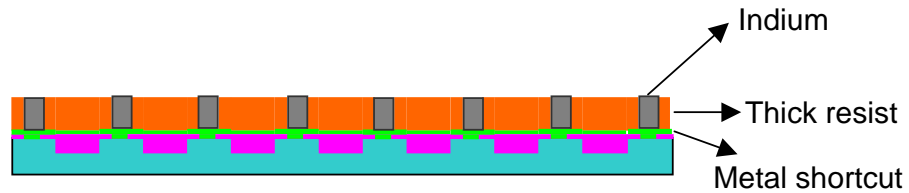


Figure 3.10 The In plated sample

Reflow

The Indium on top of the mesa structures should be reflowed by using a “Rapid Thermal Processor (RTP)” and reshaped to ball (Figure 3.11). The temperature of the sample is increased suddenly to the melting point of Indium and decreased again. So, the shape of the indium becomes to ball and the indium bumps are formed. By etching the shortcut metal, the sample will be ready for flip-chip bonding to the read-out integrated circuit.

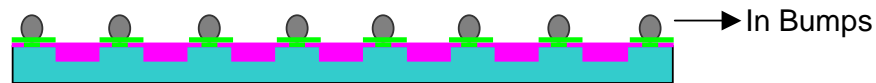


Figure 3.11 Indium bumps formed after reflow

Dicing

Before integration of detector array to the read-out circuit, the array must be separated from the support arrays. Using a dicer, the array can be diced and made ready for flip-chip.

Flip-Chip Bonding

The fabricated detector array should be integrated to the ROIC to get infrared image. The integration is done by flip-chip bonding method in this study. In this method, which is also called as direct hybrid method, the electrical connection is made with indium bumps, which provide a soft metal interconnect for each pixel. This bonding process is done by “Flip-Chip Aligner Bonder”. Figure 3.12 shows the integrated detector array and the ROIC.

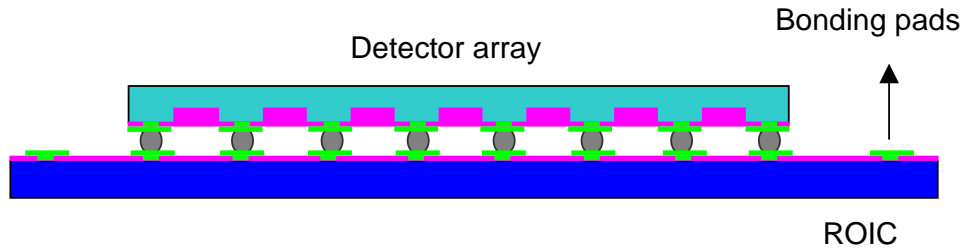


Figure 3.12 Flip-chipped detector array and read-out integrated circuit

3.2.1 Test Read-Out Circuit Fabrication

The test read-out circuit or fan-out substrate is needed for testing the fabricated test detectors. This substrate contains metal fan-outs from p and n connections of the diodes to wire bonding pads. The fabricated test detectors are flip-chip bonded to these substrates and the corresponding connections are obtained by wire bonding. Three metallization steps and a passivation process are carried out to fabricate the test read-out substrate. This substrate is fabricated from a Si wafer, whose surface is passivated by SiO_2 . Figure 3.13 shows the picture of fabricated fan-out substrate and the coupled test detector-Si fan-out substrate pair is shown in figure 3.14.

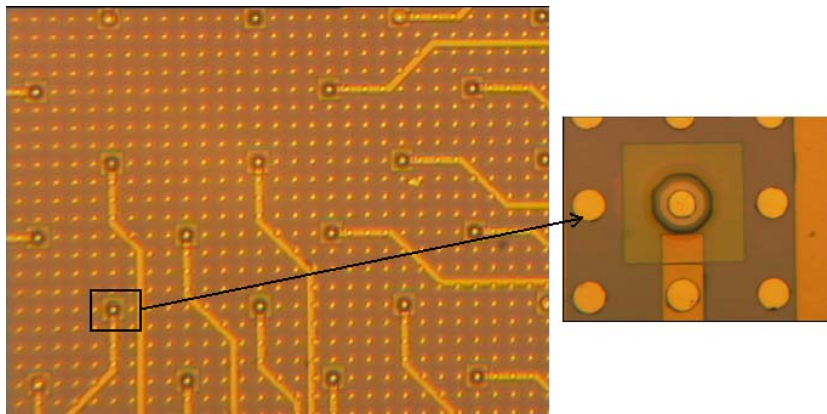


Figure 3.13 Fabricated test read-out substrate

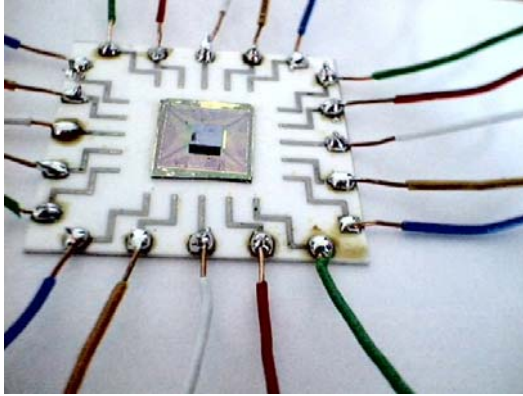


Figure 3.14 The test detector and fan-out substrate pair on an alumina substrate

3.3 Electrical Characterization

The fabrication of test photodetectors was followed by the electrical and optical characterizations of the photodetectors. The photodetectors were placed inside a cryostat cooled by CTI Cryogenics Refrigerator and I–V measurements were taken at different temperatures between 80 K and 240 K for both AlInSb/InSb/InSb heterostructure and InSb/InSb/InSb homostructure diodes. The set up used in I–V measurements can be seen in Fig. 3.15.

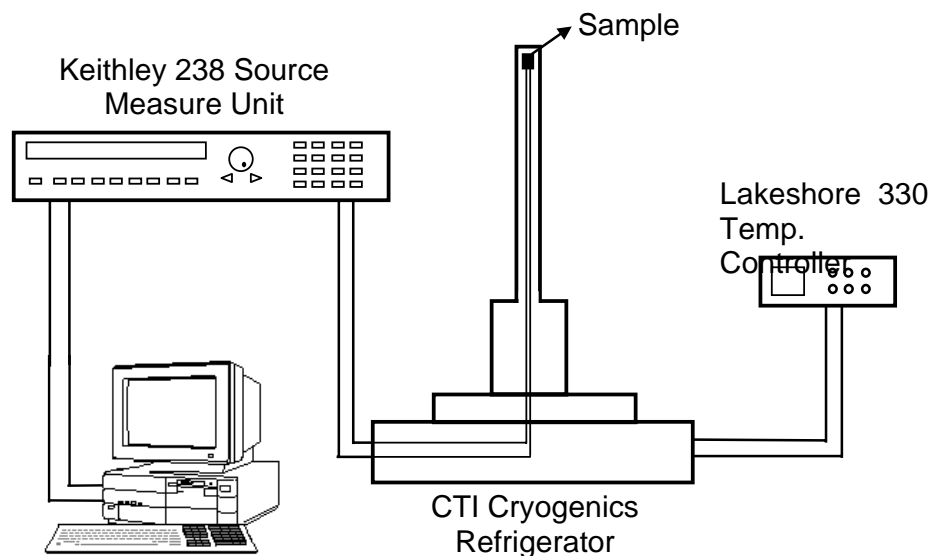


Figure 3.15 Test set up for current-voltage measurements of the detectors

Figure 3.16 and figure 3.17 show the current-voltage characteristics and the differential resistance of $33 \times 33 \mu\text{m}^2$ detectors of both structures at 77K. The zero bias differential resistances (R_0) of AlInSb/InSb/InSb and InSb/InSb/InSb structures at 77K are $210 \text{ k}\Omega$ and $90 \text{ k}\Omega$ respectively. The dark current (I_d) was measured to be $2.06 \times 10^{-8} \text{ A}$ for AlInSb/InSb structure and $1.48 \times 10^{-7} \text{ A}$ for InSb/InSb structure under a reverse bias of 0.01 V .

It is observed that, the reverse bias dependence of the differential resistance of AlInSb/InSb/InSb structure is stronger than that of the InSb/InSb/InSb structure. The detailed analysis of the dark current will be presented in section 3.4.5.

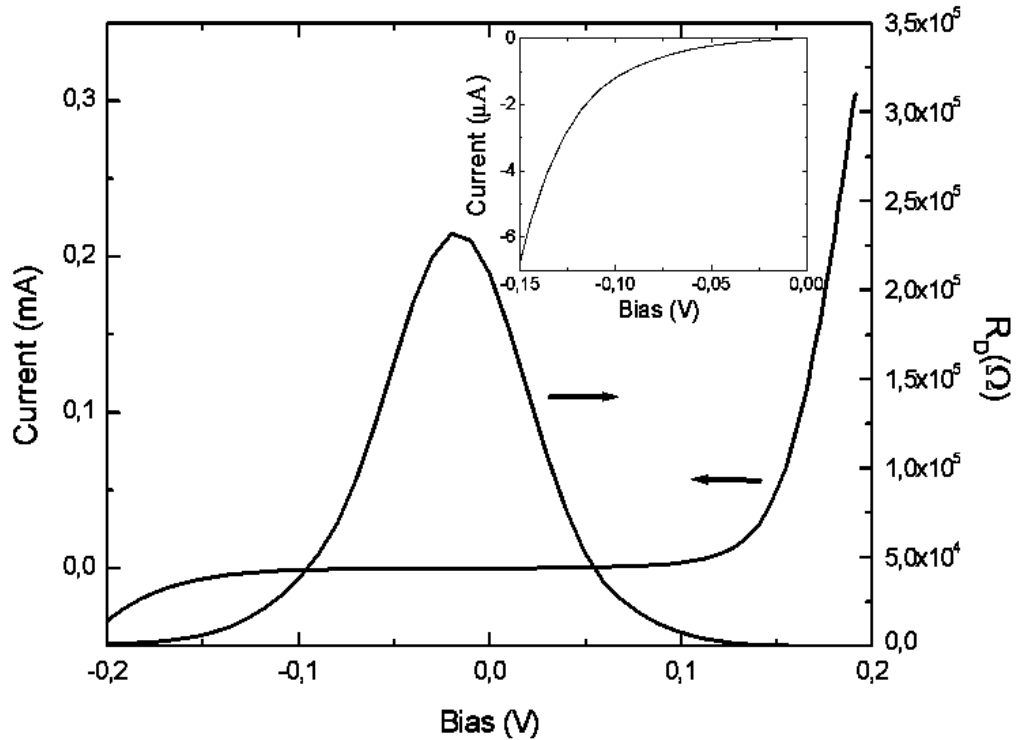


Figure 3.16 I - V characteristic and R_D of AlInSb/InSb/InSb detector at 77K

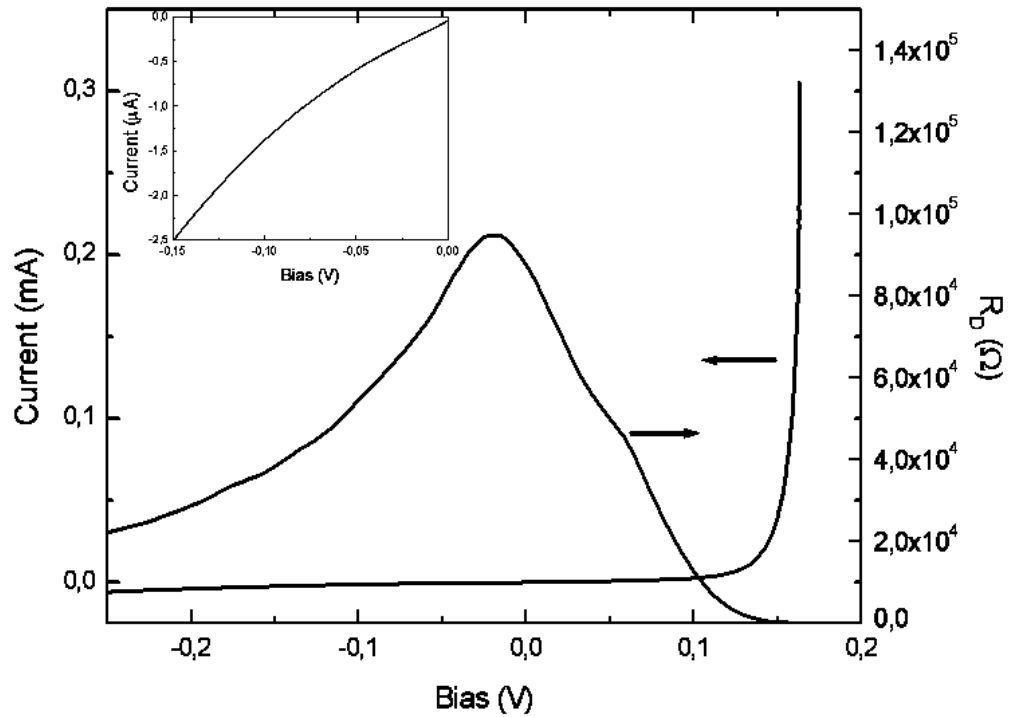


Figure 3.17 I - V characteristic and R_D of InSb/InSb/InSb detector at 77K

3.4 Dark Current

Several dark current mechanisms are important in determining the dark current voltage characteristics of a photodiode. The dark current is the superposition of the current contributions from three diode regions: bulk, depletion region, and surface.

- diffusion current in the bulk p and n regions, I_{DIF}
- generation recombination current in the depletion region, I_{G-R}
- tunneling current; band to band tunneling current, I_{BTB} and trap-assisted tunneling current, I_{TAT}
- ohmic leakage, or shunt current, I_S

Each of the above components has its own individual relationship to voltage and temperature.

3.4.1 Diffusion Current

Diffusion current is the fundamental current mechanism in a p-n junction photodiode. It results from the diffusion of thermally generated minority carriers from the quasi-neutral n- and p-regions to the junction. Diffusion current density, J_D , consists of electrons injected from the n-side over the potential barrier into the p-side and an analogous current due to holes injected from the p-side into the n-side [2].

$$J_D = J_s \left[\exp\left(\frac{qV}{kT}\right) - 1 \right] \quad 3.1$$

J_s is the saturation current density and can be defined as,

$$J_s = q \left[\frac{D_n n_p}{L_p} + \frac{D_p p_n}{L_n} \right] \quad 3.2$$

where D_n and D_p are the minority carrier diffusion constants in cm^2/sec , L_n and L_p are the minority carrier diffusion lengths in cm for electrons and holes respectively. n_p and p_n are the electron and hole minority carrier concentrations in cm^{-3} . Using the relations

$$D = \mu \frac{kT}{q} \quad 3.3$$

$$L = \sqrt{\tau D} \quad 3.4$$

$$n_i^2 = n_n p_p \quad 3.5$$

the saturation current density expression can be rewritten as

$$J_s = n_i^2 (qkT)^{1/2} \left[\frac{1}{p_p} \left(\frac{\mu_n}{\tau_n} \right)^{1/2} + \frac{1}{n_n} \left(\frac{\mu_p}{\tau_p} \right)^{1/2} \right]^{-1} \quad 3.6$$

where n_i is the intrinsic carrier concentration (cm^{-3}), μ_n , μ_p are electron and hole mobilities respectively ($\text{cm}^2/\text{V}\cdot\text{sec}$), and τ_n , τ_p are electron and hole life-times in the p and n type regions, respectively. Diffusion current varies with temperature as n_i^2 and usually is the dominant junction current at higher temperatures, but not at the operation temperatures of the low band gap semiconductor photodiodes.

3.4.2 Generation-Recombination Current

This component of the current can become the dominant dark current contributing mechanism in diodes whose depletion region has high density of Shockley-Read (S-R) centers. The S-R centers may be present in the original material used in the fabrication of diodes or these may also be created during the processing of the junction. The S-R centers within the depletion region act as intermediate states for the thermal generation and recombination of carriers. The resulting generation-recombination current density, J_{G-R} , is defined as [2]

$$J_{g-r} = \left(\frac{n_i W_o kT}{V_{bi} (\tau_e \tau_h)^{1/2}} + \frac{P s_o n_i W_o kT}{A V_{bi}} \right) \left(\frac{2 \sinh \left(\frac{qV}{2kT} \right)}{\left(\frac{V_{bi} - V}{V_{bi}} \right)^{1/2}} \right) f(b) \quad 3.7$$

where τ_e and τ_h are the carrier lifetimes of electrons and holes respectively, V is the applied bias, W_o is the zero bias depletion layer width, s_o is the surface recombination velocity, V_{bi} is the built-in potential, P and A are the perimeter and the area of the diode. $f(b)$ is

$$f(b) = \int_0^{\infty} \frac{du}{u^2 + 2bu + 1} \quad 3.8$$

where

$$b = \exp\left(-\frac{qV}{2kT}\right) \cosh\left(\frac{E_t + E_i}{kT} + \frac{1}{2} \ln\left(\frac{\tau_h}{\tau_e}\right)\right) \quad 3.9$$

with E_i and E_t intrinsic and trapping energy levels, respectively.

3.4.3 Tunneling Current

The third type of dark current component that can exist is a tunneling current caused by electrons directly tunneling across the junction from the valance band to the conduction band (Band-to-Band Tunneling) or by electrons indirectly tunneling across the junction by way of intermediate trap states in the junction region (Trap-Assisted Tunneling).

Band-to-Band Tunneling

Band-to-band tunneling (BTB) originates due to the direct tunneling of carriers under the influence of relatively high reverse bias in narrow band gap semiconductors. At relatively higher bias voltages, the electrons directly tunneling from the valance band on the n-side are responsible for band-to-band tunneling current. In dark current modeling, a simple approach for BTB current expression can be used [45].

$$J_{BTB} = \frac{q}{4\eta\pi^2} \left[\frac{E_g kT}{P^2} \right]^{1/2} \int_{-E_{\max}}^0 T_p\left(\frac{E}{2}\right) dE \quad 3.10$$

where, $E_{\max} = -qV + E_F$, P is the momentum matrix, E_F is the Fermi energy, and T_p is the tunneling probability.

$$T_p = \exp \left[- \left(\frac{2m_e}{\eta^2} \right)^{1/2} \left(\frac{2\epsilon_0\epsilon_s}{q^2 N_d} \right)^{1/2} E_g \left\{ \left(1 - \frac{E}{E_g} \right) \left[\frac{\pi}{2} - \sin^{-1} \left(\frac{-E}{E_g - E} \right)^{1/2} \right] - \left(-\frac{E}{E_g} \right)^{1/2} \right\} \right] \quad 3.11$$

Trap-Assisted Tunneling

It has its origin in the tunneling of minority carriers from occupied trap states located either in the depletion region or in the quasi-neutral region very close to the depletion edge to the empty band states on the other side of the junction. The expression for the dark current density due to trap-assisted tunneling is [46]

$$J_{TAT} = qN_t \left[\frac{c_p p_1 w N_c}{c_p p_1 + w N_c} \right] x_d \quad 3.12$$

where N_t is the trap density, x_d is the depletion layer width, c_p is the capture coefficient of holes, $p_1 = N_v \exp \left[-\frac{E_t}{kT} \right]$, N_v is the density of states in the valence band, E_t is the trap energy level, and wN_c is the tunneling rate. It can be seen from equation 3.12 that the trap-assisted tunneling current can be formed from two different mechanisms: thermal mechanism and tunneling mechanism. In this study, it is assumed that the trap-assisted tunneling is limited by tunneling from trap level. In this case

$$c_p p_1 \gg w N_c \quad 3.13$$

Then, the TAT current expression will be simplified to

$$J_{TAT} = qN_t (w N_c) x_d \quad 3.14$$

The tunneling rate is

$$wN_c = \frac{\pi^2 q m_e^* E M^2}{h^3 (E_g - E_t)} \exp \left[-\frac{4(2m_e^*)^{1/2} (E_g - E_t)^{3/2}}{3\eta q E} \right] \quad 3.15$$

where M is the matrix element of the trap potential, m_e^* is the effective mass of electrons, and E is the electric field associated with the tunneling barrier.

3.4.4 Ohmic Leakage Current

This component of the current is responsible for exhibiting a shunt-leakage behavior in junction performance and owes its origin to surface leakage current and dislocations intersecting the junction. The current-voltage characteristics of a p-n junction often exhibit an excess current component, a part of which can be modeled as an ohmic current component given by [45],

$$I_{sh} = \frac{V}{R_{sh}} \quad 3.16$$

where V is the applied voltage across the junction and R_{sh} is the diode shunt resistance.

3.4.5 Analysis of Dark Current

In order to identify the dominant dark current mechanisms in the corresponding bias and temperature regions, the measured differential resistance values are fitted to theoretical formulations. The following R_D expressions for diffusion, generation-recombination, trap assisted tunneling and ohmic leakage mechanisms for InSb/InSb/InSb homojunction diodes were used.

$$(R_{DIFF})^{-1} = C_{DIFF} \exp\left(-\frac{qV}{kT}\right) \quad 3.17$$

$$C_{DIFF} = \frac{1}{AJ_s} \quad 3.18$$

$$(R_{GR})^{-1} = \frac{1}{C_{GR}} \frac{\partial f(V, T)}{\partial V} \quad 3.19$$

$$f(V, T) = \left(\frac{2 \sinh\left(\frac{qV}{2kT}\right)}{\left(\frac{V_b - V}{V_b}\right)^{1/2}} \right) f(b) \quad 3.20$$

$$\frac{1}{C_{GR}} = A \left(\frac{n_i w_o kT}{V_b \tau_o} + \frac{P s_o n_i w_o kT}{AV_b} \right) \quad 3.21$$

$$(R_{TAT})^{-1} = C_{TAT1} \exp\left(\frac{C_{TAT2}}{(V_b - V)^{1/2}}\right) \left(1 - \frac{C_{TAT2}}{2(V_b - V)^{1/2}}\right) \quad 3.22$$

$$C_{TAT1} = \frac{q^2 A \pi^2 m_v M^2}{h^3 (E_g - E_t)} N_t \quad 3.23$$

$$C_{TAT2} = -\frac{4(2m_v)^{1/2} (E_g - E_t)^{3/2}}{3q\eta \left(\frac{qN_d}{2\varepsilon}\right)^{1/2}} \quad 3.24$$

All the fitting parameters, which are C_{DIFF} , C_{GR} , C_{TAT1} and C_{TAT2} , are bias independent. They include the semiconductor parameters and the temperature. In the fitting procedure, some parameters were assumed to be independent of both bias and temperature. By inserting $q=1.6 \times 10^{-19}$ C, $k=1.38 \times 10^{-23}$ J/K, $A=1.1 \times 10^{-5}$ cm²

(diode area), $P=1.32 \times 10^{-2}$ cm (peripheral), $s_o=1 \times 10^4$ cm/sec (surface recombination velocity), $m_v=3.75 \times 10^{-31}$ kg, $N_D=1 \times 10^{18}$ cm⁻³, $h=6.626 \times 10^{-34}$ Js, $\epsilon=1.49 \times 10^{-10}$ F/m into the above expressions, excellent fit was obtained in a large reverse bias and temperature range. N_t is the trap density and can be extracted from C_{TATI} after fitting. The built-in potential V_b , band gap energy E_g , intrinsic carrier concentration n_i , and the depletion layer width w_o are temperature dependent parameters and are obtained from the below equations [2,47] and tabulated in table 3.2 for heterojunction detector.

$$E_g(T) = 0.235 - \frac{3.4 \times 10^{-4} T^2}{210 + T} \quad 3.25$$

$$n_i = (3.12 + 2.69 \times 10^{-3} T) \times 10^{14} T^{3/2} E_g^{3/4} \exp\left(-\frac{qE_g}{2kT}\right) \quad 3.26$$

$$V_b = \frac{kT}{q} \ln\left(\frac{N_A N_D}{n_i^2}\right) \quad 3.27$$

$$w_o = \left[\frac{2\epsilon V_b}{q} \left(\frac{1}{N_A} + \frac{1}{N_D} \right) \right]^{1/2} \quad 3.28$$

Table 3.2 The calculated values of fitting parameters for different temperatures for AlInSb/InSb/InSb heterostructure detector

T (K)	E_g (eV)	n_i (m⁻³)	V_b (V)	W_o (m)
80	0.2275	5.65x10 ¹⁵	0.2260	2.92x10 ⁻⁷
120	0.2202	3.68x10 ¹⁸	0.2052	2.78x10 ⁻⁷
160	0.2115	1.13x10 ²⁰	0.1796	2.61x10 ⁻⁷
200	0.2018	9.72x10 ²⁰	0.1507	2.39x10 ⁻⁷

The integration in equation 3.8 was calculated numerically from -0.3 V to 0.05 V range at 5 mV steps for different temperatures. While doing these calculations, the trap energy level (E_t) was assumed to be equal to intrinsic energy level (E_i) and the electron generation-recombination lifetime (τ_e) was also assumed to be equal to hole generation-recombination lifetime (τ_h), in order to make $f(b)$ to be independent of material parameters for the simplification of the calculation.

For AlInSb/InSb/InSb heterostructure detectors, in addition to the above dark current components, the band-to-band tunneling (BTB) current mechanism was also taken into account to have a better fit. The BTB differential resistance expression can be written as [46]

$$(R_{BTB})^{-1} = C_{BTB1} \exp\left[-\frac{C_{BTB2}}{(V_b - V)^{1/2}}\right] \left[(V_b - V)^{1/2} + \frac{C_{BTB2}}{4}\right] \quad 3.29$$

where,

$$C_{BTB1} = \frac{3}{2} \times 10^{-2} N_A^{1/2} A \quad 3.30$$

$$C_{BTB2} = \frac{4 \times 10^{10} E_g^2}{N_A^{1/2}} \quad 3.31$$

The total differential resistance is parallel combination of all resistance components.

$$\frac{1}{R_D} = \frac{1}{R_{DIFF}} + \frac{1}{R_{GR}} + \frac{1}{R_{TAT}} + \frac{1}{R_{BTB}} + \frac{1}{R_{SHUNT}} \quad 3.32$$

Figures 3.18 and 3.19 show the measured change in the differential resistance with respect to bias voltage in the temperature range of 80 K- 240 K for both detectors. Excellent results were obtained by numerical fitting of the sum of the differential resistance components to experimental data over a range of both applied voltage and temperature.

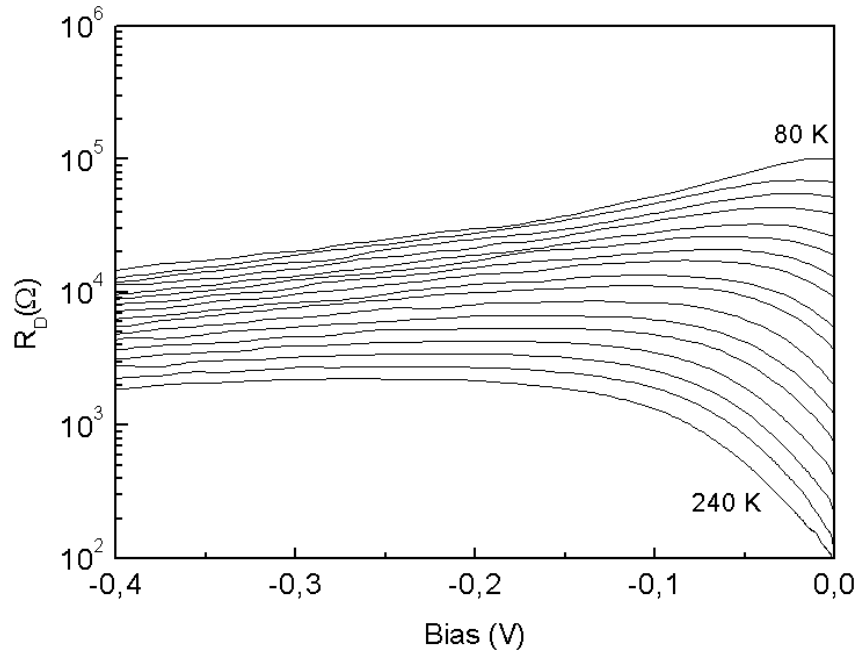


Figure 3.18 R_D vs. V graph of InSb/InSb/InSb from 80K to 240K [48]

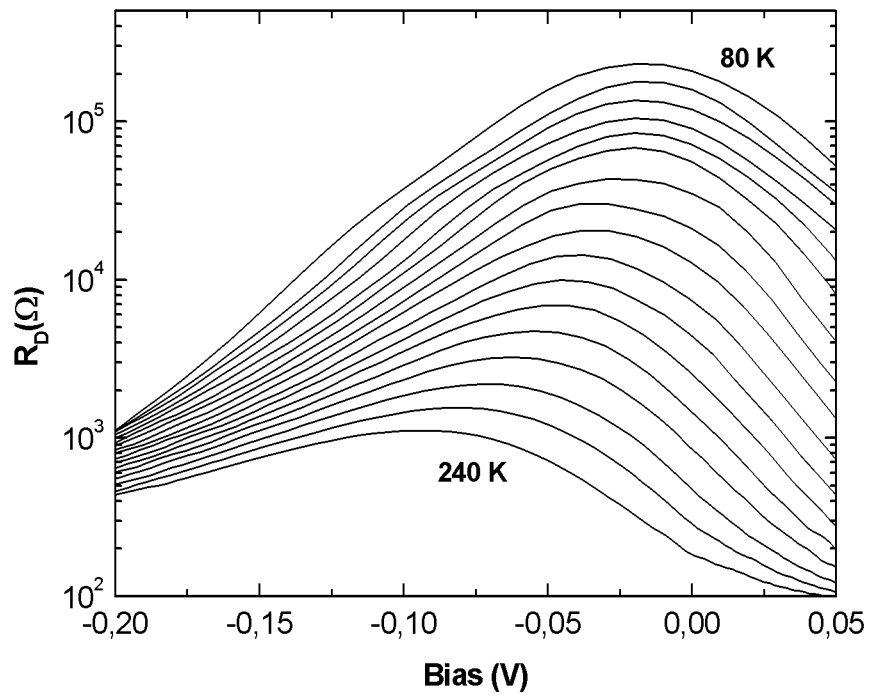


Figure 3.19 R_D vs. V characteristics of AlInSb/InSb/InSb from 80K to 240K.

As it can be seen from figure 3.20, shunt and trap-assisted-tunneling components of the differential resistance are dominant throughout the entire bias range shown at 80 K for InSb/InSb/InSb p-i-n detector. For the heterojunction AllnSb/InSb/InSb detector, unlike the homojunction one, band-to-band mechanism is also at considerable level and it limits R_D for reverse bias voltages larger than 200mV. In HgCdTe detectors, BTB mechanism is the dominant mechanism at higher reverse bias and low temperatures [49]. From -200mV to near zero bias, the R_D of the heterojunction detector is dominated by TAT mechanism while shunt resistance is the performance limiting component near zero bias at 80K. Under small forward bias, the generation-recombination mechanism is the dominant component. It can be seen from figures 3.20 and 3.21 that, the rate of change of the differential resistance of the heterojunction detector with bias is relatively higher than that of the homojunction detector in the reverse bias region.

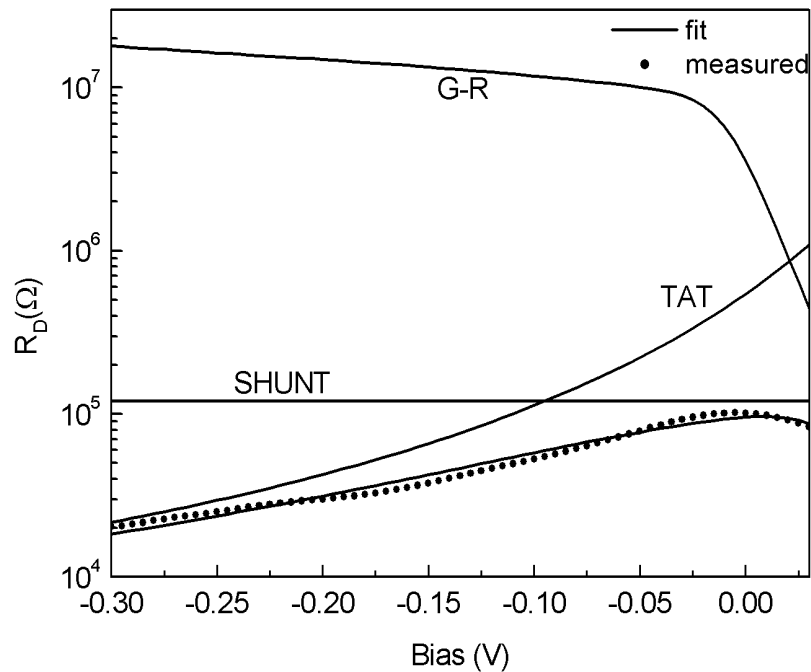


Figure 3.20 The fitting result of R_D for InSb/InSb/InSb detectors at 80K [48].

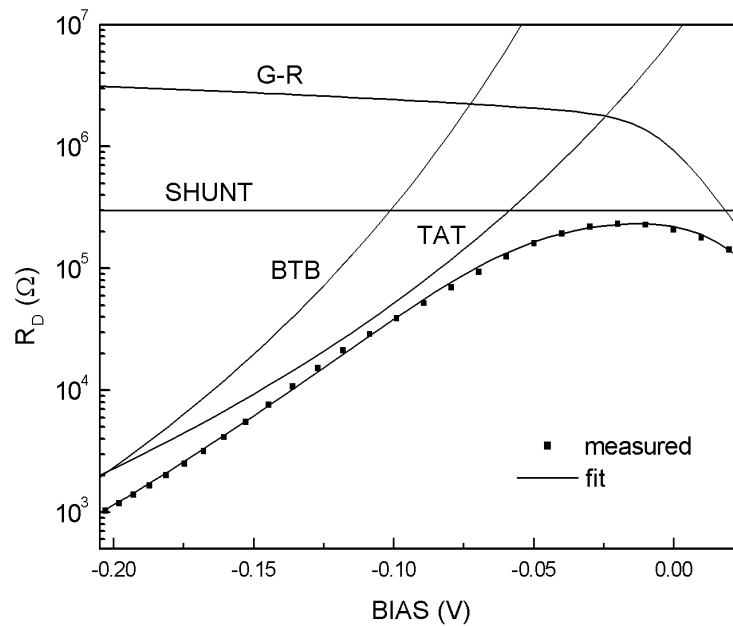


Figure 3.21 The fitting result of R_D for AlInSb/InSb/InSb detectors at 80K.

Figures 3.22 and 3.23 show the fitting results for the homojunction and heterojunction detectors respectively at 80K, 120K, 160K, and 200K. In the homojunction diode case, above ~ 160 K, the generation-recombination mechanism replaces the TAT and shunt components as the dominant component of the dark current. Also, diffusion appears as the resistance limiting mechanism in forward bias region at ~ 200 K. The AlInSb/InSb/InSb heterojunction diode shows similar dominant dark current mechanisms at low temperatures. However, due to presumably higher trap density in this photodiode, TAT is still the dominant mechanism the high reverse bias region at 200 K.

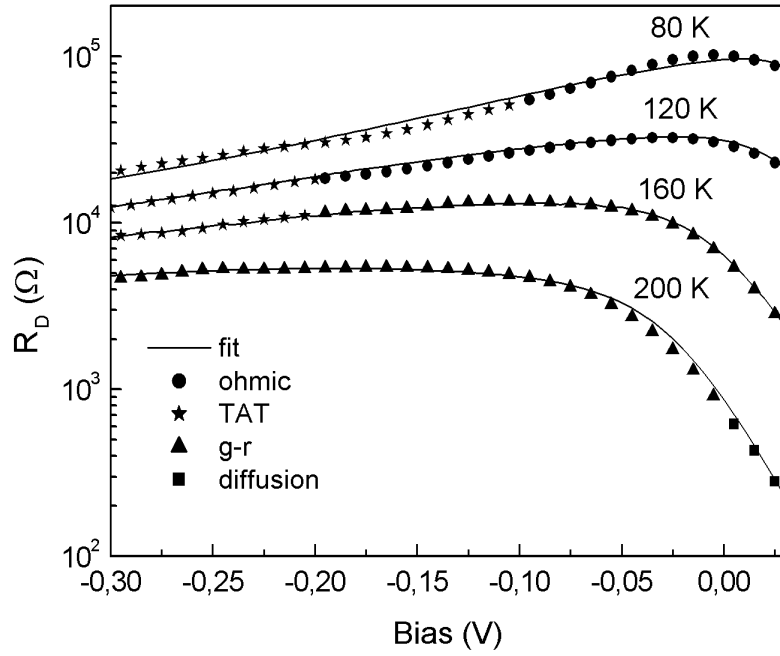


Figure 3.22 Fitting results of InSb/InSb detector at different temperatures [48].

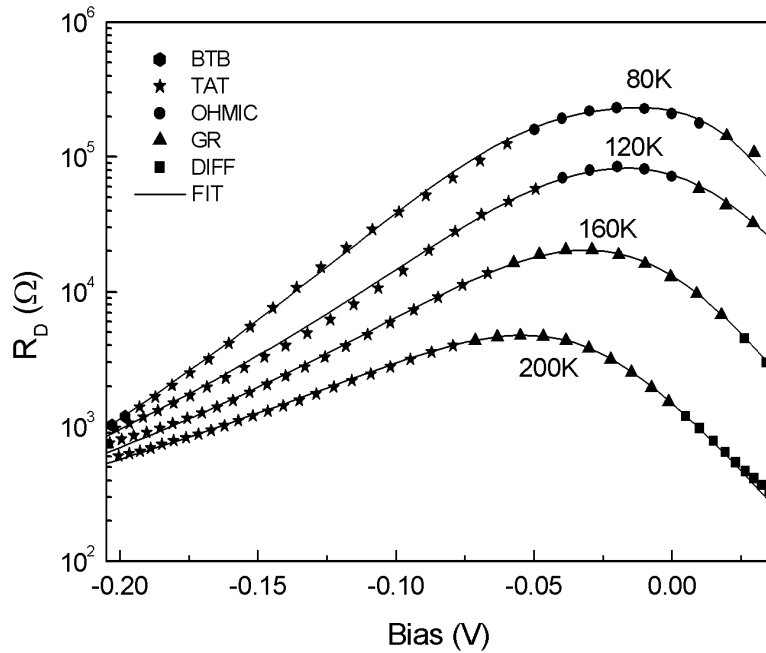


Figure 3.23 Fitting results of AlInSb/InSb/InSb at different temperatures.

The effective depletion layer generation-recombination lifetime (τ_o), and the active trap density (N_t) of the detectors can be found from equations 3.21 and 3.24 respectively, after finding the values for the coefficients of C_{G-R} , C_{TAT1} , C_{TAT2} . The effective depletion layer generation-recombination lifetime (τ_o) for heterojunction and homojunction detectors were found as 0.1ns and 0.2 ns respectively at 120K. The active trap density (N_t) is $1.79 \times 10^{17} \text{ cm}^{-3}$ for AlInSb/InSb and $1.55 \times 10^{15} \text{ cm}^{-3}$ for InSb/InSb detectors at 80K temperature.

Figures 3.23 and 3.24 show the change of the differential resistance with the temperature for both detectors. At high temperatures and around zero bias, the activation energies were calculated as $\sim 200\text{meV}$, which is close to the band gap energy of InSb, confirming that the zero-bias differential resistance is limited by diffusion mechanism under high temperatures, for both structures. Note that the resistance is limited by the shunt leakage under small reverse bias for both diodes. The shunt resistance displays small activation energy of around 25 mV as seen in Figures 3.24 and 3.25 showing that the temperature dependence of the shunt resistance is weaker than that of intrinsic carrier concentration.

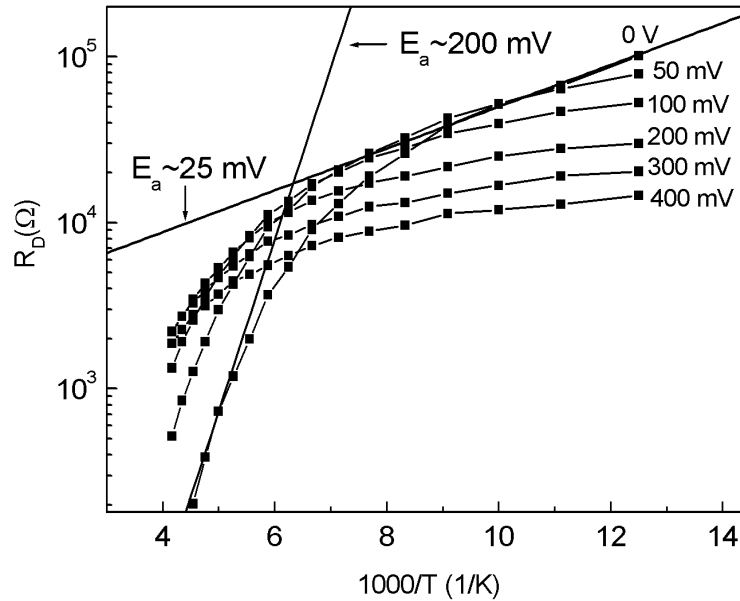


Figure 3.24 R_D vs. T for InSb/InSb/InSb at different bias voltages [48].

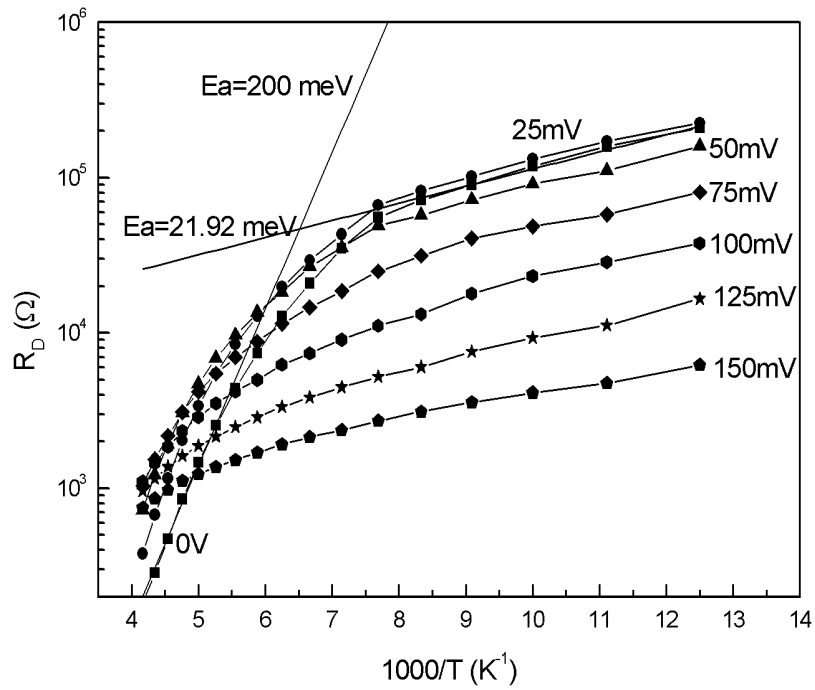


Figure 3.25 R_D vs. T for AlInSb/InSb/InSb at different bias voltages.

3.5 Detector Noise

The noise measurements were performed for AlInSb/InSb/InSb detector at different bias and temperatures in the frequency range of 10-4000 Hz using the Agilent 4395A Network/Spectrum/Impedance Analyzer and a preamplifier. Figure 3.26 shows the equivalent circuit of the measurement set-up.

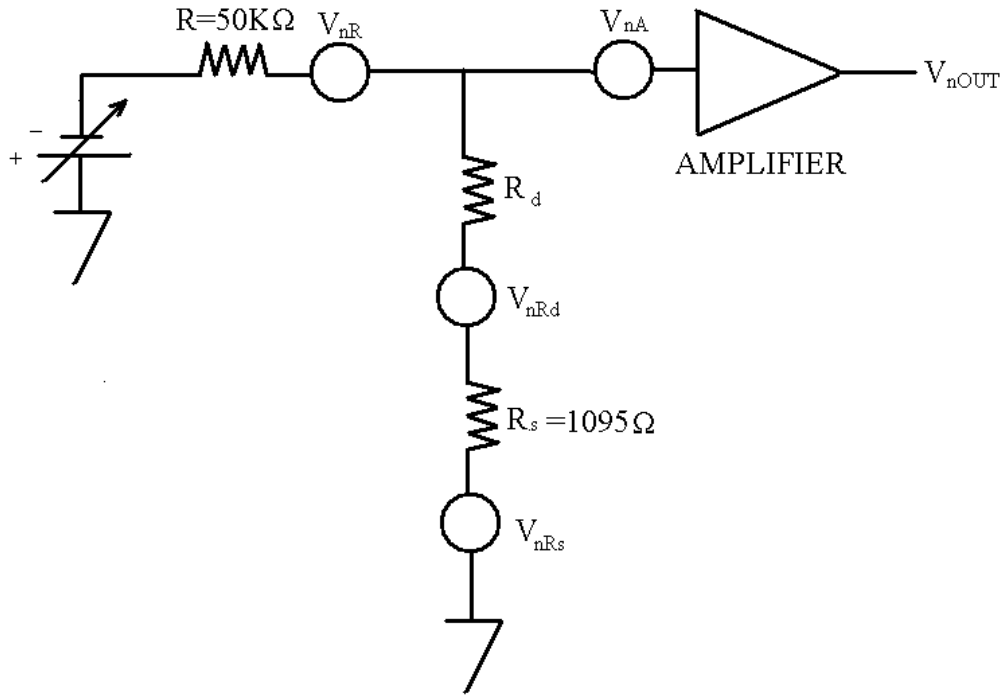


Figure 3.26 Equivalent circuit for noise measurement.

At zero bias, no $1/f$ noise was observed for all temperatures. The measured output noise contains all the components from different sources, such as amplifier noise and thermal noise of the resistors. The $1/f$ noise of the detector was obtained by extracting the unwanted noise components from the measured output noise using the following equation

$$\left(\frac{V_{nOUT}}{A}\right)^2 = V_{nOP}^2 + \left[\frac{V_{nR}(R_D + R_S)}{R + R_D + R_S}\right]^2 + \left[\frac{V_{nRd}R}{R + R_D + R_S}\right]^2 + \left[\frac{V_{nRs}R}{R + R_D + R_S}\right]^2 \quad 3.33$$

where A is the amplifier gain ($A=1000$), V_{nOP} is the amplifier noise and

$$V_{nR} = \sqrt{4kTqR} \quad 3.34$$

is the thermal noise of a resistor.

After extracting the $1/f$ noise of the detector, the noise at 1 Hz was found by extrapolating the data to this frequency. The change of noise spectral density at 1 Hz with bias voltage was plotted in order to investigate the contribution of dark current components to $1/f$ noise. The results are shown in Fig.3.27.

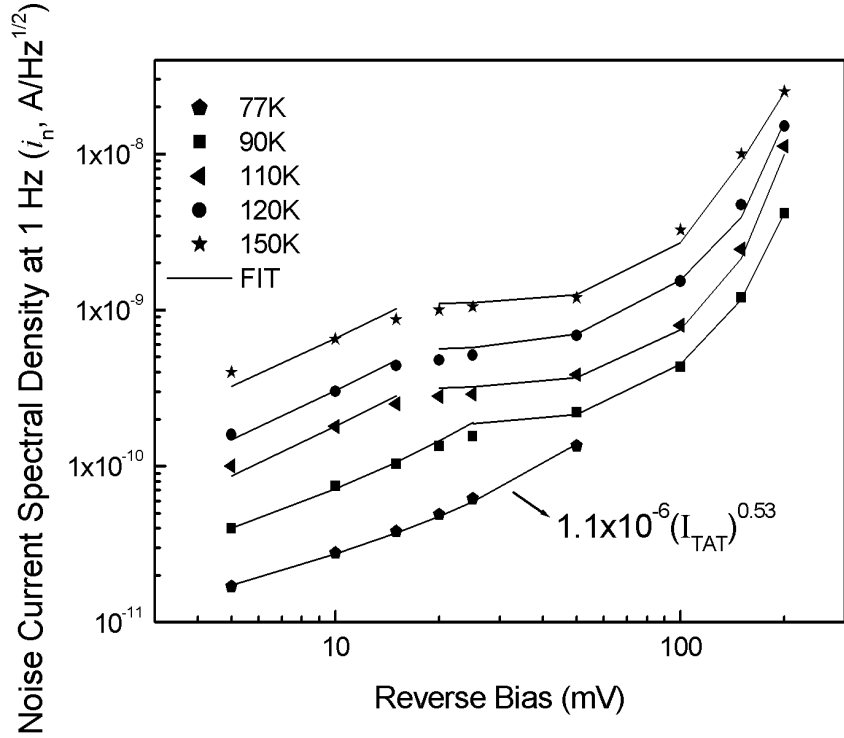


Figure 3.27 Reverse bias dependence of $1/f$ noise of AlInSb/InSb/InSb detector

The TAT mechanism was expected to be the dominant dark current component contributing to $1/f$ noise at 77K. Confirming this expectation, the measured $1/f$ noise gives an excellent fit to

$$i_n = \alpha_{TAT} (I_{TAT})^\beta \quad 3.35$$

with $\alpha_{TAT} = 1.1 \times 10^{-6}$ and $\beta = 0.53$ at 80 K. These values are close to values found by Nemirovsky and Unikovsky [50] for HgCdTe photodetectors and Besikci *et al.* [16] for InAsSb photodiodes ($\alpha_{TAT} = 1 \times 10^{-6}$ and $\beta = 0.5$). At higher temperatures,

the noise current tends to saturate when the reverse bias exceeds 20 mV and then increases significantly with the bias. This shows that, different components dominate the noise current at small and high reverse bias regions. Bajaj *et al.* [51] observed the saturation of the noise current at around 50mV reverse bias for HgCdTe photodiodes which was in disagreement with the theory proposed by Kleinpenning in [52].

Kleinpenning [53] suggests a model for $1/f$ noise spectral density for the depletion region generation-recombination noise as

$$S_I(f) = \frac{2\alpha q I}{3f\tau} \left[1 - \exp\left(-\frac{qV}{kT}\right) \right] \quad 3.36$$

where α is the Hooge's parameter, I is the G-R current, f is the frequency, and τ is the carrier lifetime. However, for high reverse bias regions, equation 3.36 must be modified [54]. The maximum noise power spectral density for G-R noise at high reverse bias regions is [53]

$$S_I^{\max}(f) = \frac{4\alpha q I v_s}{3fW^*} \quad 3.37$$

In the above expression, v_s is the carrier saturation velocity and W^* is the effective width of space charge region.

The fit results obtained by using Kleinpenning's model together with $i_{nTAT} = \alpha_{TAT} (I_{TAT})^{\beta_{TAT}}$ and $i_{nBTB} = \alpha_{BTB} (I_{BTB})^{\beta_{BTB}}$ are shown in Figure 3.27 and 3.28. Figure 3.28 shows the noise components contributing to the total noise of the heterojunction detector at 90K and 120K. At 90K and low reverse bias region (0-20mV), both TAT and G-R components have contributions to $1/f$ noise while G-R is the limiting mechanism at higher temperatures. The generation-recombination domination of the noise current can be explained by Kleinpenning's model. At

moderate reverse bias regions (20mV-50mV), G-R noise current saturates but is still the dominant component of the spectral noise for the temperatures higher than 90K. Above 100 mV, the rate of increase in the noise current with bias is larger than that predicted by $i_n = \alpha_{TAT} (I_{TAT})^\beta$ with $\alpha = 1.1 \times 10^{-6}$ and $\beta = 0.53$ (Figure 3.28).

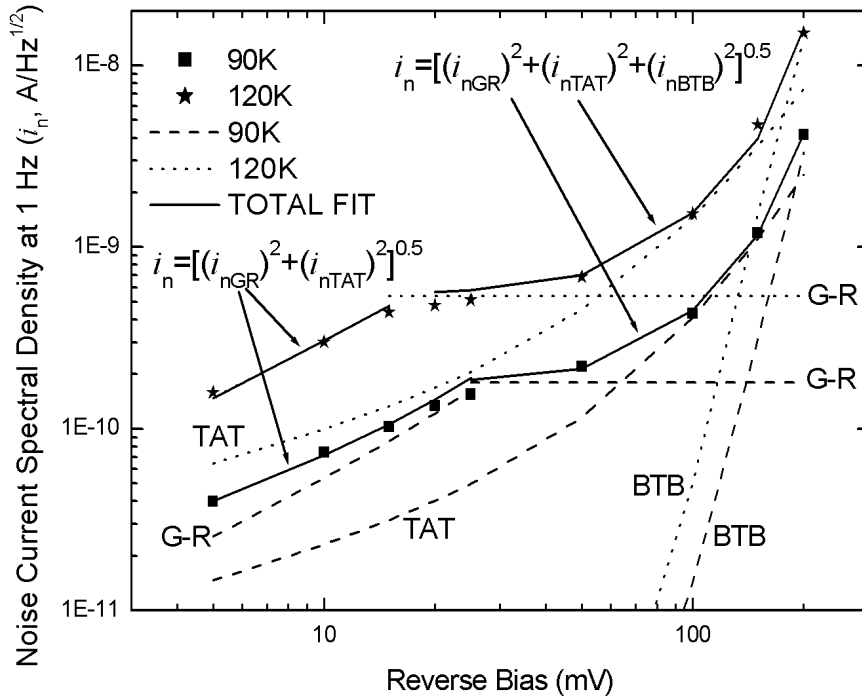


Figure 3.28 The components contributing to total I/f noise for AlInSb/InSb/InSb detector at 90K and 120K

The fit at this region can be improved by including an additional component, which is band-to-band tunneling. In this region, where there is a considerable contribution of band-to-band tunneling in addition to trap-assisted tunneling, the I/f noise current is associated with the two components of the tunneling current and includes BTB as well as TAT. In this range, BTB introduced I/f noise was modeled as $i_n = \alpha_{BTB} (I_{BTB})^\beta$ with $\alpha = 2 \times 10^{-3}$ and $\beta = 0.98$. Similar parameters for BTB

tunneling introduced $1/f$ noise current were observed by Nemirovsky and Unikovsky [50].

3.6 Optical Characterization

After electrical characterization, the detector array was placed in a liquid nitrogen cooled-dewar for optical characterization. The dewar vacuum jacket was at 10 mbar vacuum level before the liquid nitrogen was poured into the container. The test setup, which is shown in figure 3.29, was established and the responsivity and the noise of the detector arrays were measured. In this setup the commercial blackbody source was heated to 500 °C temperature and the radiation is modulated at 515 Hz via a chopper blade just in front of the 0.6-inch blackbody aperture. The dewar was 25 cm away from the aperture and mounted on a xyz stage. The dewar window is uncoated ZnSe window which is suitable for the MWIR and LWIR ranges. The transmission of the window is 80% near the region of spectral interest. The radiation was normally incident to the detector surface. The measurement was carried out by backside illumination and without substrate thinning and anti-reflection coating of the detectors. The detector hybrid was connected to the cold surface with thermally conductive epoxy. The fan-out die of the detector hybrid was connected to the Al₂O₃ substrate with gold leads. The pads on the Al₂O₃ substrate were connected to the hot cables, which were guided out to the dewar electrical port. The signal from the detector was first preamplified with a two-stage transconductance amplifier. The bias was kept around zero by the preamplifier. Once the signal is preamplified, it is fed to the 10Mohm-voltage input of a lock-in amplifier (Stanford Research SR810) with 50 ohm coaxial cable and BNC connector. The lock-in amplifier receives the TTL reference signal from the optical chopper controller and measures within the 1-2 Hz bandwidth of the reference signal at 515 Hz. The lock-in amplifier is a DSP processor type and automatically sets the filter parameters and time constants for the best possible measurement. It then displays the signal voltage at the chopped frequency in V_{rms} units. Dividing

this signal to the preamplifier gain, detector impedance and optical power incident on to the detector, the current responsivity of the detector was obtained in A/W.

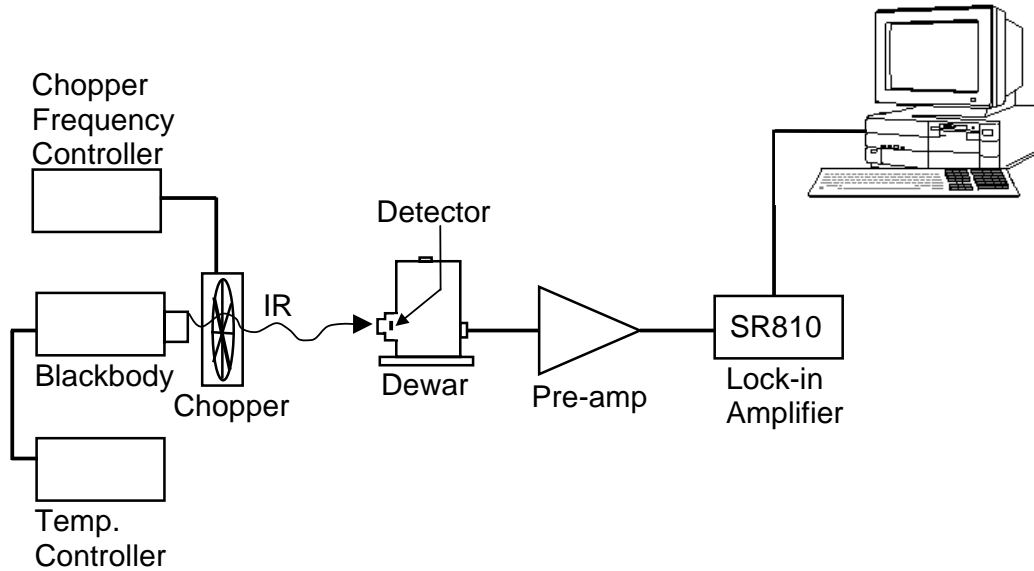


Figure 3.29 Responsivity and noise measurement setup

The spectral response of the detectors under zero bias was measured at 77 K using the setup shown in figure 3.30. The Fourier transform interferometer (FTIR) is a Michelson interferometer type instrument, which sends the infrared radiation to a detector from a blackbody source after modulating the light with itself. The detector response is measured with an analog to digital converter. This signal is the response of the system in position space. Taking the Fourier transform of this signal gives the response of the detector in wave number space hence spectral response can be obtained from this information. Before performing the experiment, the measurement setup was calibrated by using a commercial pyroelectric DTGS detector. This spectrum is recorded and stored in memory. After that, the detector under interest is measured, and its raw spectrum is divided to previously stored and referenced spectrum. This eliminates the absorption and other effects in the instrument chamber since the DTGS response is flat in the spectral region of interest. The wavelength range of the system is 1 μm -20 μm band. The lower limit was due to FTIR scanner accuracy and the higher limit is due to pyroelectric reference detector cutoff.

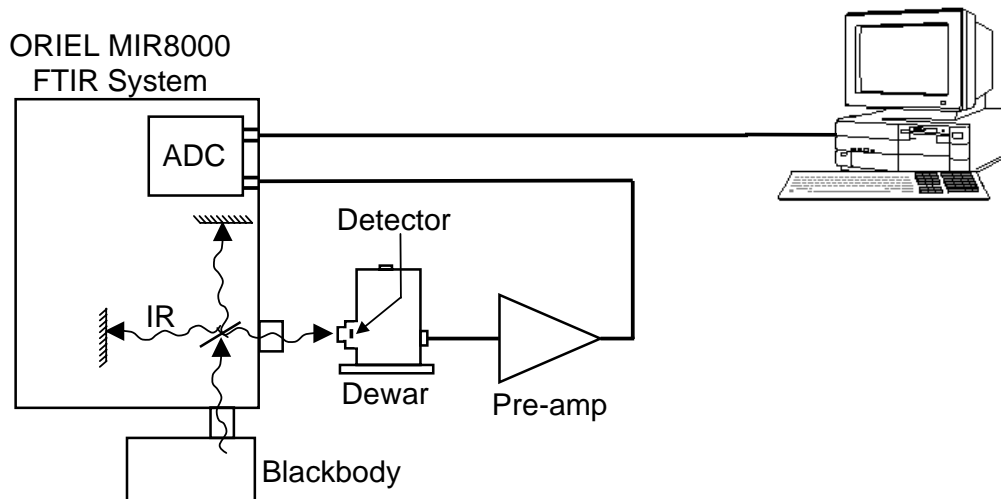


Figure 3.30 Detector spectral response measurement setup

Figure 3.31 and 3.32 show the spectral responses of $33 \times 33 \mu\text{m}^2$ AlInSb/InSb/InSb and InSb/InSb/InSb detectors respectively. The measured peak detectivity of the heterostructure detector is $\sim 7 \times 10^9 \text{ cmHz}^{1/2}/\text{W}$ at 77 K, while the peak detectivity of InSb/InSb/InSb detectors is $\sim 1 \times 10^{10} \text{ cmHz}^{1/2}/\text{W}$.

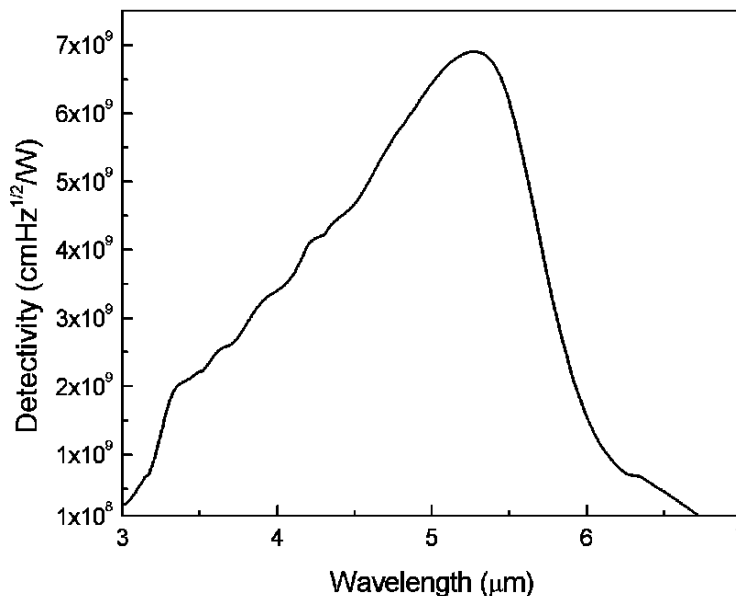


Figure 3.31 The spectral response of AlInSb/InSb/InSb detector at 80 K.

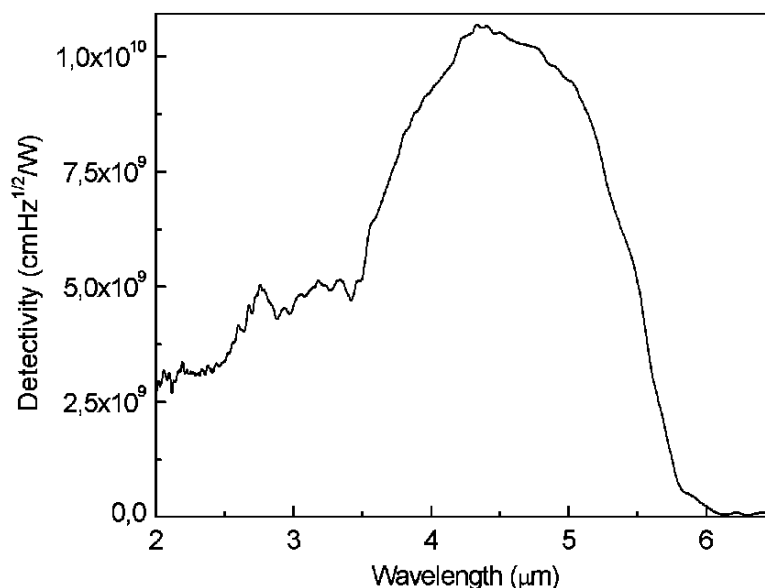


Figure 3.32 The spectral response of InSb/InSb/InSb detector at 80 K.

If we compare these two detectors, we see that, the optical performance of the homojunction detector is better than the other one, although the zero bias differential resistance of the heterostructure detector is better. Higher noise spectral density of the heterostructure detector results in a relatively low detectivity.

The spectral response of both detectors in the shorter wavelengths ($<4\mu\text{m}$) is very small compared to the spectral response in the wavelength range around $5\mu\text{m}$ (Figures 3.31 and 3.32). The short wavelength spectral response of both detectors, which are backside illuminated, decreases with large dislocation density at the substrate/epilayer interface [55]. This is probably due to Shockley-Read recombination associated with the dislocations. The large lattice mismatch between Si substrate and InSb epilayer (19%) causes large dislocation density at the interface and the shorter wavelength photons will be absorbed closer to this interface. Therefore, the spectral response at shorter wavelengths of both heterojunction and homojunction detectors decreases as the minority carrier diffusion length decreases with high dislocation density at the Si substrate/InSb epilayer due to large lattice mismatch.

CHAPTER IV

128x128 ARRAY FABRICATION AND TESTING

After characterizing the test detectors, 128x128 AlInSb/InSb/InSb detector arrays were fabricated and tested for getting real time infrared images. This chapter contains the fabrication of the 128x128 arrays and performing real time thermal imaging with the fabricated arrays. The fabrication and characterization of the 128x128 arrays were performed at the Electrical and Electronics Engineering Department of METU in collaboration with Selcuk Ozer.

4.1 Fabrication of 128x128 Detector Arrays

Focal plane array fabrication is more complex and consists of additional processes compared to the fabrication of test detectors. The fabrication processes explained in Chapter 3 were used to fabricate the detector arrays. Starting by etching the mesa structures, the array fabrication continues with a series of metallization and passivation processes and ends by In plating. The standard photolithographic technique was used by employing Karl-Süss MA56 as the mask aligner in all processes. A positive type photoresist was spun using a homemade spin coater in all processes. The coated photoresist was baked in the oven and developed using standard developers. After photolithography, the undeveloped very thin photoresist residues were removed from the sample by using oxygen and argon

plasmas successively in Bio-Rad PT7150 Plasma Barrel Etcher/Asher, which is necessary for the following etching, passivation, or metallization steps. The metal depositions were performed by resistive thermal evaporation in NANOTECH THIN FILM model evaporator and the lift-off process was done by placing the sample into extra pure acetone and using BANDELIN SONOREX 10P digital ultrasonic cleaner.

Firstly, the sample was cleaned by hot acetone, isopropyl alcohol, and DIW in the ultrasonic cleaner. Then, the mesa etching process was performed and the samples were etched down to n^+ doped InSb layer. The dimension of the mesa structures is $33\ \mu\text{m} \times 33\ \mu\text{m}$. (Figure 4.1).

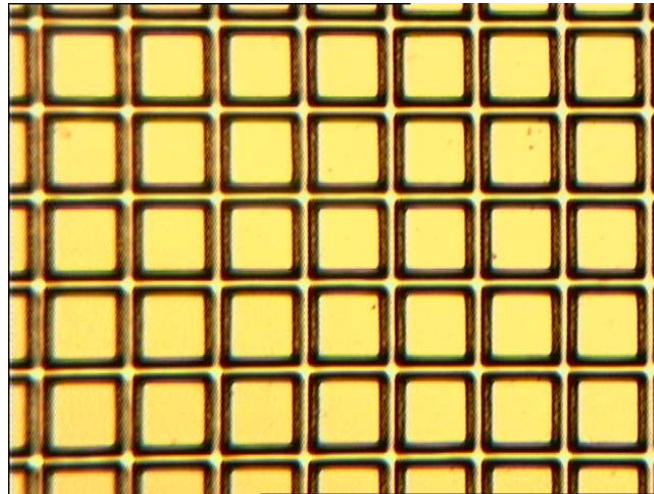


Figure 4.1 The picture of etched mesa structures

Later, the detectors in the array were passivated and ohmic contacts were formed on top of the detectors. After evaporation of the ohmic contacts, the indium plating was implemented for flip-chip bonding. Then, reflow was done so that the plated indium becomes ball-shaped (Figure 4.2).

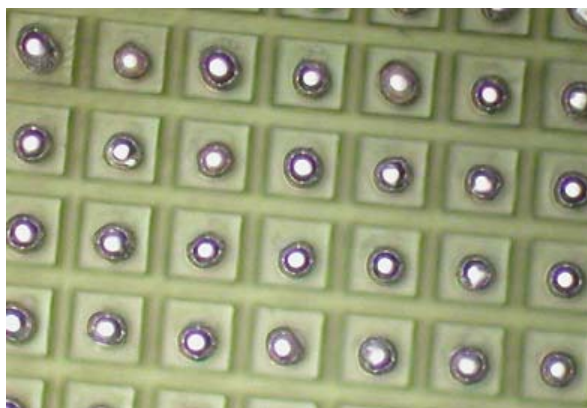


Figure 4.2 The fabricated array with indium bumps

After finishing the fabrication steps, the 128x128 array detectors were diced to integrate with the read-out integrated circuits (ROICs). The integration process was done using RD Automation M8AN model Flip-chip Aligner & Bonder. The flip-chip bonded detector array and the ROIC were placed in an LCC package as shown in figure 4.3 for thermal imaging using a laboratory type thermal imager.

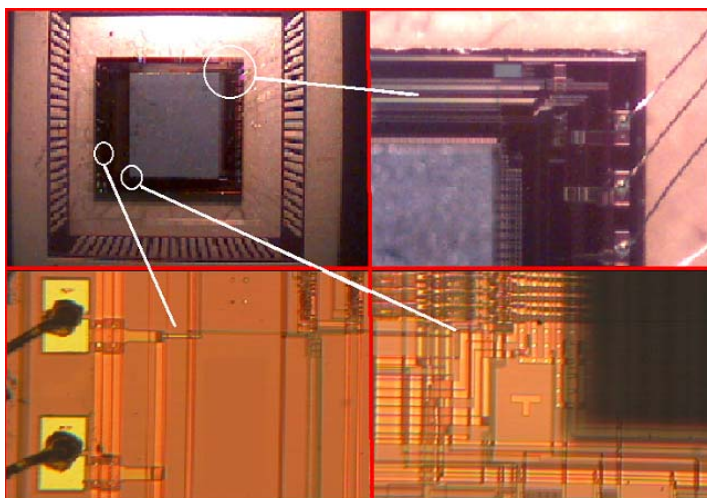


Figure 4.3 Flip-chip integrated detector array and ROIC were placed in LCC package

4.2 Real Time Thermal Imaging

The fabricated detector array was inserted in a thermal imager for testing the performance of the array. The thermal imager has a liquid nitrogen cooled dewar and a 3-5 μm Ge lens with 50mm focal length, 5.5° field of view and f number of 2.3. The laboratory type imager performs 8-bit normalization. Figure 4.4 shows the image of candlelight with colors mapping to different temperatures.

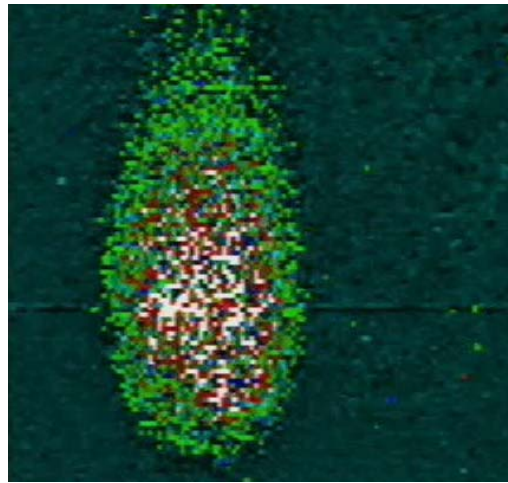


Figure 4.4 Infrared image of candlelight from 128x128 AlInSb/InSb/InSb heterojunction detector

Due to the high dark current, the detector array is capable of thermal imaging objects with temperatures higher than ~ 340 K. While the detector performance is significantly lower than that of a commercial InSb detector array on InSb substrate, as to our knowledge, this is the first study on thermal imaging with a heterojunction InSb detector on Si substrate, and the results are encouraging. In order to improve the performance, growth conditions and the detector layer structure must be optimized to decrease the defect density in the epilayers.

CHAPTER V

CONCLUSION

In this study, p-i-n InSb/InSb/InSb homojunction and AlInSb/InSb/InSb single heterojunction epilayers grown on Si substrates were used for infrared detector performance analysis. Small arrays of $33 \times 33 \mu\text{m}^2$ detectors were fabricated from these materials for electrical and optical characterization and noise measurements. In addition, 128×128 format detector arrays were fabricated for real time infrared imaging. The measured zero bias differential resistances are $90 \text{ k}\Omega$ and $210 \text{ k}\Omega$ for homojunction and heterojunction detectors respectively. A peak 80 K detectivity as high as $1 \times 10^{10} \text{ cmHz}^{1/2}/\text{W}$ was achieved for InSb homojunction detectors on Si substrate in spite of the large lattice mismatch between Si and InSb (19%). The measured 80 K peak detectivity of the heterojunction detector was $7 \times 10^9 \text{ cmHz}^{1/2}/\text{W}$.

The dark current, which is one of the most important parameters in the photodetector characterization, was analyzed for heterojunction detectors and compared with that of homojunction detectors. The contribution of dark current mechanisms to total dark current was studied for different temperature and bias ranges by fitting the measured data to theoretically calculated data. Excellent fits were obtained for differential resistance of the detectors. At 80 K, R_D is dominated by shunt resistance around zero bias and by TAT at moderately high reverse bias

regions for both detectors. Unlike homojunction detector, the domination of the differential resistance by band-to band tunneling was observed in the heterojunction detector. In addition, the change of R_D with bias voltage in AlInSb/InSb detector is much faster than that of InSb/InSb homojunction detector. This is due to higher trap density (N_t) at the junction region of the heterojunction detector.

At temperatures higher than 120 K, the generation recombination replaces the shunt mechanism as the dominant dark current component around zero bias, and at higher temperatures (>150K), diffusion current is the limiting mechanism of the differential resistance under forward bias for both detectors.

The spectral noise for AlInSb/InSb structure was studied at different reverse bias voltages and temperatures. At 80K, the I/f noise is dominated by TAT mechanism, and the noise current at 1 Hz is in good agreement with the empirical relation of $\alpha_{TAT}(I_{TAT})^{\beta_{TAT}}$ with $\alpha_{TAT}\sim 1\times 10^{-6}$ and $\beta_{TAT}\sim 0.5$ in the whole bias region. However, at higher temperatures (>100K) and higher reverse bias (>50mV) regions, the contribution of band-to-band tunneling process to noise current was also observed with the coefficients of $\alpha_{BTB}=2\times 10^{-3}$ and $\beta_{BTB}=0.98$. At higher temperatures, the slope of the noise current changes rapidly at low bias regions, indicating the G-R contribution to the I/f noise. At these temperatures and bias regions, the G-R noise mechanism was explained by Kleinpenning's model [53].

The final study of this thesis was obtaining real time infrared images from AlInSb/InSb/InSb detector arrays fabricated in the format of 128x128. For this purpose, the detector was placed into a laboratory infrared imager and cooled by liquid nitrogen. Only hot objects, whose temperatures are larger than 340K, were thermally imaged due to the high dark current of the detector. However, as to our knowledge, this is the first thermal image taken by AlInSb/InSb/InSb p-i-n on Si substrate in the world. By optimizing the growth conditions and detector layer structures to decrease the defect density in the epilayers, the performance of the detectors can be improved.

REFERENCES

- [1] J.D. Vincent, *Fundamentals of Infrared Detector Operation and Testing*, Wiley Press, Santa Barbara Research Center, 1990.
- [2] A. Rogalski, *Infrared Photon Detectors*, SPIE Press, Washington, 1995.
- [3] J. Zeigler, M. Bruder, M. Finck, R. Krüger, P. Menger, Th. Simon, R. Wollrab, *Infrared Physics and Technology* 43 (2002) 239-243.
- [4] D.A. Scribner, M.R. Kruer, and J.M. Killiany, *Proceedings of the IEEE* Vol 79 (1991) 66-85
- [5] A. Rogalski, *Infrared Physics and Technology* 43 (2002) 187-210.
- [6] W. Cabanski, R. Breiter, R. Koch, W. Gross, K.-H. Mauk, W. Rode, J. Ziegler, H. Schneider, M. Walter, R. Oelmaier, *Infrared Physics and Technology* 43 (2002) 257-263.
- [7] J.L. Tissot, *Infrared Physics and Technology* 43 (2002) 223-228.
- [8] H.C. Liu, F. Capasso, *Intersubband Transitions in Quantum Wells*, Academic Press, San Diego, 2000.
- [9] M.B. Reine, A.W. Hairston, P. O'Dette, S.P. Tobin, F.T. Smith, B.L. Musicant, P. Mitra, F.C. Case, *Proc. SPIE*, Vol. 3379 (1998) 200-212.
- [10] S.D. Gunapala, S.V. Bandara, A. Singh, J.K. Liu, S.B. Rafol, E.M. Luong, J.M. Mumolo, N.Q. Tran, J.D. Vincent, C.A. Shott, J.F. James, P.D. Levan, *Proc. SPIE*, Vol. 3698 (1999) 687-697.
- [11] J.D. Kim, S. Kim, D. Wu, J. Wojkowski, J. Xu, J. Piotrowski, E. Bigan and M. Razeghi, *Applied Physics Letters* 67 (1995) 2645-2647
- [12] J.D. Kim, D. Wu, J. Wojkowski, J. Piotrowski, J. Xu, and M. Razeghi, *Applied Physics Letters* 68 (1996) 99-101

- [13] A. Rakovska, V. Berger, X. Marcadet, B. Vinter, G. Glastre, T. Oksenhendler, and D. Kaplan, *Applied Physics Letters* 77 (2000) 397-399
- [14] X. Marcadet, A. Rakovska, I. Prevot, G. Glastre, B. Vinter, V. Berger, *Journal of Crystal Growth* 227-228 (2001) 609-613.
- [15] W. Dobbelaere, J. De Boeck, P. Heremans, R. Mertens, G. Borghs, W.Luyten, and J. Van Landuyt, *Applied Physics Letters* 60 (1992) 3256-3258.
- [16] C. Besikci, S. Ozer, C. Van Hoof, L. Zimmermann, J. John, and P. Merken, *Semiconductor Science and Technology* 16 (2001) 992-996.
- [17] C.G. Bethea, M.Y.Yen, K.K. Coi, and A.Y Cho, *Applied Physics Letters* 51 (1988) 1431-1432.
- [18] C.G. Bethea, B.F. Levine, M.Y.Yen, and A.Y Cho, *Applied Physics Letters* 53 (1988) 291-292.
- [19] K. Mohammed, F. Capasso, A. Logan, P. Van Der Ziel, L. Hutchinson, *Electronics Letters* 22 (1986) 215-216.
- [20] J.D. Kim, H. Mohseni, J.S. Wojkowski, J.J. Lee, and M. Razeghi, 'Photodetectors: Materials and Devices IV' *SPIE Vol.3629* (1999) 338-348.
- [21] J.S. Wojkowski, H. Mohseni, J.D. Kim, and M. Razeghi, 'Photodetectors: Materials and Devices IV' *SPIE Vol. 3629* (1999) 357-363.
- [22] A. Rakovska, V. Berger, X. Marcadet, B. Vinter, G. Glastre, K. Bouzehouane, D. Kaplan, T. Oksehendler, 'Photodetectors: Materials and Devices V' *SPIE Vol. 3948* (2000) 55-62.
- [23] M. Kudo and T. Mishima, *Japanese Journal of Applied Physics* 37 (1998) 1132-1134
- [24] A. Tevke, C. Besikci, C. Van Hoof, and G. Borghs, *Solid-State Electronics* Vol. 42 (1998) 10361044.
- [25] E. Michel, J. Xu, J.D. Kim, I. Ferguson, and M. Razeghi, *IEEE Photonics Technology Letters* Vol. 8 (1996) 673-675.
- [26] A. Kepten, Y. Shacham-Diamand, and S.E. Shacham, 'Infrared Detectors: State of the Art' *SPIE Vol.1735* (1992) 277-286.
- [27] A. Kepten, Y. Shacham-Diamand, and S.E. Shacham, 'Infrared Detectors and Focal Plane Arrays' *SPIE Vol.1685* (1992) 305-316.

- [28] C.T. Elliot, 'Infrared Technology and Applications XXII' SPIE Vol. 2744 (1996) 452-462.
- [29] J.J. Lee, J.D. Kim, and M. Razeghi, Applied Physics Letters 70 (1997) 3266-3268.
- [30] J.J. Lee, J.D. Kim, and M. Razeghi, Applied Physics Letters 71 (1997) 2298-2300.
- [31] K.Y. Ma, Z.M. Fang, D.H. Jaw, R.M. Cohen, and G.B. Stringfellow, Applied Physics Letters 55 (1989) 2420-2422.
- [32] K.T. Huang, C.T. Chiu, R.M. Cohen, and G.B. Stringfellow, Journal of Applied Physics 75 (1993) 2857-2863.
- [33] A.J. Noreika, W.J. Takei, M.H. Francombe, and C.E.C. Wood, Journal of Applied Physics 53 (1982) 4932-4937.
- [34] Q. Du, J. Alperin, and W.I. Wang, Journal of Crystal Growth 175/176 (1997) 849-852.
- [35] Y.H. Choi, C. Besikci, R. Sudharsanan, and M. Razeghi, Applied Physics Letters 63 (1993) 361-363.
- [36] Y.H. Choi, P.T. Staveteig, E. Bigan, and M. Razeghi, Journal of Applied Physics 75 (1993) 3196-3198.
- [37] J.J. Lee and M. Razeghi, Applied Physics Letters 76 (2000) 297-299.
- [38] M. Van Schilfgaarde, A. Sher, and A. Chen, Applied Physics Letters 62 (1993) 1857-1859.
- [39] P.T. Staveteig, Y.H. Choi, G. Labeyrie, E. Bigan, and M. Razeghi, Applied Physics Letters 64 (1994) 460-462.
- [40] J.D. Kim, E. Michel, S. Park, J. Xu, S. Javadpour, and M. Razeghi, Applied Physics Letters 69 (1996) 343-344.
- [41] M. Van Schilfgaarde, A. Chen, S. Krishnamurthy, and A. Sher, Applied Physics Letters 65 (1994) 2714-2716.
- [42] I. Vurgaftman and J.R. Meyer, Journal of Applied Physics 81 (2001) 5815-5874.
- [43] S.M. Sze, *VLSI Technology*, McGraw-Hill, New York, 1983.
- [44] M. Köhler, *Etching in Microsystem Technology*, Wiley-VCH Verlag GmbH, Weinheim, 1999.

- [45] V. Gopal, S.K. Singh, R.M. Mehra, *Infrared Physics and Technology* 43 (2002) 317-326.
- [46] Y. Nemirovsky, R. Fastov, M. Meyassed, A. Unikovsky, *Journal of Vacuum Science and Technology B9* (1991) 1829-1839
- [47] B.G. Streetman, *Solid State Electronic Devices*, Prentice Hall, New Jersey, 1995.
- [48] S. Ozer and C. Besikci, *Journal of Physics D: Applied Physics* 36 (2003) 559-563.
- [49] Y. Nemirovsky, D. Rosenfeld, R Adar, and A. Kornfeld, *Journal of Vacuum Science and Technology A7* (1989) 528-535.
- [50] Y. Nemirovsky and A. Unikovsky, *Journal of Vacuum Science and Technology B10* (1992) 1602-1610.
- [51] J. Bajaj, E.R. Blazejewski, G.M. Williams, and R.E. DeWames, *Journal of Vacuum Science and Technology B10* (1992) 1617-1625.
- [52] T.G.M. Kleinpenning, *Journal of Vacuum Science and Technology A3* (1985) 176-xxx.
- [53] T.G.M. Kleinpenning, *Physica B* 154 (1988) 27-34.
- [54] L.K.J. VanDamme, and B. Orsal, *IEEE Transactions on Electron Devices* Vol. 35 (1988) 502-506.
- [55] S.M. Johnson, D.R. Rhiger, J.P. Rosbeck, J.M. Peterson, S.M. Taylor, and M.E. Boyd, *Journal of Vacuum Science and Technology B10* (1992) 1499-1506.
- [56] K. Jowikowski and A. Rogalski, *Journal of Electronic Materials* 29 (2000) 736-741.